Biophysical Journal
Article

Biophysical Society

Hydrophobic Mismatch Modulates Stability and Plasticity of Human Mitochondrial VDAC2

Shashank Ranjan Srivastava,[1] Punit Zadafiya,[1] and Radhakrishnan Mahalakshmi[1,*]
[1]Molecular Biophysics Laboratory, Department of Biological Sciences, Indian Institute of Science Education and Research, Bhopal, India

ABSTRACT The human mitochondrial outer membrane protein voltage-dependent anion channel isoform 2 (hVDAC2) is a β-barrel metabolite flux channel that is indispensable for cell survival. It is well established that physical forces imposed on a transmembrane protein by its surrounding lipid environment decide protein structure and stability. Yet, how the mitochondrial membrane and protein-lipid interplay together regulate hVDAC2 stability is unknown. Here, we combine experimental biophysical investigations of protein stability with all-atom molecular dynamics simulations to study the effect of the most abundant mitochondrial phosphocholine (PC) lipids on hVDAC2. We demonstrate experimentally that increasing the PC lipid acyl chain length from *di*C14:0 to *di*C18:0-PC has a nonlinear effect on the β-barrel. We show that protein stability is highest in *di*C16:0-PC, which exhibits a negative mismatch with the hVDAC2 barrel. Our simulations also reveal that structural rigidity of hVDAC2 is highest under optimal negative mismatch provided by *di*C16:0-PC bilayers. Further, we validate our observations by altering the physical properties of PC membranes indirectly using cholesterol. We propose that VDAC plasticity and stability in the mitochondrial outer membrane are modulated by physical properties of the bilayer.

INTRODUCTION

Cellular biomembranes possess a dynamic phospholipid bilayer, harboring membrane proteins that carry out vital functions for cell survival. In humans, although transmembrane proteins are largely helical in nature, transmembrane β-barrels are present almost exclusively in the outer mitochondrial membrane (OMM) (1). The OMM possesses a distinct composition of phospholipids with trace amounts of cardiolipin and cholesterol. The physicochemical nature of these lipids influence membrane protein energetics (2). Therefore, lipid-dependent regulation forms a vital component of membrane protein function, stability, and oligomerization (3,4). Previous studies have identified the role of bilayer lateral pressure and bilayer stress, membrane asymmetry, protein-lipid hydrophobic mismatch, and curvature stress on the oligomerization of transmembrane helices (4–6), in providing a signaling platform, and also causing unfavorable aggregation (7,8). Similar studies on transmembrane β-barrels are limited (1,7) and have suggested that the rigidity of β-barrel proteins do not allow for considerable structural plasticity in a mismatched bilayer (9,10).

We asked if the OMM modulates the energetics of its most abundant β-barrel channel, namely the human voltage-dependent anion channel (hVDAC). Humans have three VDAC isoforms that adopt 19-stranded β-barrel structures. They additionally possess a flexible N-terminal voltage-sensor helix that docks within the folded barrel (11–13). hVDAC1 and hVDAC2 are vital for metabolite and nutrient flux (13–15). In particular, the hVDAC2 isoform has gained considerable recent interest owing to its antiapoptotic properties, its potential involvement in forming the permeability transition pore, and its relevance to neurodegeneration and cardiomyopathies (13,15–17). Cholesterol is believed to affect VDAC dynamics (18–20). VDAC oligomerization and gating are also influenced by the surrounding lipid (21–24). Although several studies focus on the role of VDACs in apoptosis and their cholesterol and cardiolipin dependence, no study has explicitly addressed the effect of phospholipids on VDAC stability.

The OMM is enriched with phospholipids, with >50% of the lipid content being phosphocholine (PC). The interplay and inter-regulation of hVDACs and PC lipids has been postulated but not explored in detail. The crystal structures of VDACs suggest that the hydrophobic thickness of this β-barrel is ~2.34 nm (25–28). When compared with documented values of hydrophobic thickness of lipid bilayers (~2.6 nm for *di*14:0 PC, ~2.9 nm for *di*16:0 PC, and ~3.2 nm for *di*18:0 PC (29)), an optimal hydrophobic match for VDACs is provided by *di*14:0 PC. However, 14-C lipids constitute <0.1% of the OMM. Hence, the molecular basis

Submitted July 9, 2018, and accepted for publication November 1, 2018.
*Correspondence: maha@iiserb.ac.in
Editor: Dimitrios Stamou.
https://doi.org/10.1016/j.bpj.2018.11.001

of VDAC-lipid interplay in the OMM calls for a detailed study.

Here, we combine experimental measurements of protein stability with all-atom molecular dynamics simulations (MDSs) of hVDAC2 to understand the effect of acyl chain length on this transmembrane β-barrel. Surprisingly, we find that the diacyl 16:0 phosphocholine (*di*C16:0-PC, DPPC) system confers the highest stability to hVDAC2 by providing an optimal negative mismatch with the transmembrane region of the barrel. The addition of cholesterol lowers hVDAC2 stability in *di*C16:0-PC lipids indirectly by increasing the membrane thickness. We propose that cells can regulate the stability of hVDAC2 in the mitochondrial outer membrane by altering the physical characteristics of the lipid bilayer.

MATERIALS AND METHODS

Lipids

All lipids and detergents were procured from Avanti Polar Lipids, Alabaster, AL. The 12C detergent used was *n*-dodecylphosphocholine (DPC), and the saturated long-chain lipids used were 1,2-dimyristoyl-*sn*-glycero-3-phosphocholine (*di*C14:0-PC, DMPC), 1,2-dipalmitoyl-*sn*-glycero-3-phosphocholine (*di*C16:0-PC, DPPC), and 1,2-distearoyl-*sn*-glycero-3-phosphocholine (*di*C18:0-PC, DSPC).

Unfolded protein stock

Purified protein powder (expressed in *Escherichia coli* and purified without any additional tag, using reported methods (30); see Fig. S1 for purification profile and sodium dodecyl sulfate polyacrylamide gel electrophoresis image) was dissolved in 6 M guanidinium chloride and 10 mM dithiothreitol (DTT) at 60°C for 5 min. Samples were centrifuged for 1 h at 4°C to remove trace amounts of undissolved protein, and the supernatant was used for folding. The protein concentration was adjusted to 250 μM. A molar extinction coefficient of 36,900 M^{-1} cm^{-1} calculated at 280 nm was used for determining the concentrations.

Protein folding in PC bicelles

The folded hVDAC2 full-length protein was prepared by two methods: indirect folding (hVDAC2 was folded in micelles, followed by reconstitution hVDAC2-micelle assembly into bicelles) or direct folding (folding of hVDAC2 into preformed bicelles). Details of the indirect folding method are provided in the Supporting Materials and Methods. The thermal parameters measured for hVDAC2 from both preparations were similar. Hence, all the experiments were performed by hVDAC2 directly folded in preformed bicelles.

Bicelles of $q = 1$ were prepared by mixing 20 mM of the respective long-chain lipid with 20 mM DPC as the short-chain lipid. Bicelles were prepared in 0.9 volume of buffer A containing 10 mM DTT by subjecting the lipid suspension to repeated freeze-thaw cycles using liquid nitrogen and 60°C heating block (42°C for DMPC bicelles) till the solution became transparent. Once formed, the bicelles were prechilled at 4°C and used for hVDAC2 reconstitution.

Direct reconstitution of protein in bicelles was achieved by a 10-fold dilution of 250 μM of 0.1 volume of the unfolded protein stock prepared in guanidinium chloride into 0.9 volumes of the prechilled bicelles. The bicelle-protein assembly was subjected to three rounds of heating (35°C), cooling (4°C), and vortexing (30 s) cycles and then allowed to equilibrate overnight at 4°C by gentle mixing at 15 rotations per minute. This sample was further diluted fivefold in buffer A (50 mM sodium phosphate (pH 7.2), 100 mM NaCl) and subjected to centrifugation at 13,500 rotations per minute, 4°C for 1 h to remove trace amounts of aggregated protein. Folding of hVDAC2 was verified using the fluorescence emission spectra in bicelles and single-channel-gating measurements in a planar bilayer membrane using an electrophysiology set-up, using reported methods (30,31) (Fig. S2). The final folding mixture had 5 μM protein, 4 mM DPC, and 4 mM long-chain lipid to achieve a bicelle $q = 1.0$ in buffer A containing 2 mM DTT.

Cholesterol doping in PC bicelles

The different long-chain PC lipids (DMPC, DPPC, DSPC) in chloroform were doped with different percents (w/v) of cholesterol (0.02, 0.03, and 0.04% with respect to the long-chain lipid) and dried under a stream of nitrogen, followed by lyophilization. Bicelles of $q = 1.0$ having varying percentage of cholesterol were prepared as described above, with DPC as the short-chain lipid. A negligible amount of lipid was lost in the case of DSPC:DPC bicelles with 0.02% cholesterol. Occasionally, protein folding efficiency was affected in the 0.04% cholesterol-doped condition. The conversion between percent w/v and mole percent is presented in Table S2.

Differential scanning microcalorimetry

Bicelles are known to exhibit complex phases that are temperature dependent. To verify whether this interfered in our measurements, bicelles of different q (0.5, 0.75, and 1.0) and varying chain lengths (14-C, 16-C, 18-C) were prepared in buffer A. DPC was used as the short-chain lipid. The enthalpic transitions of these bicelles were monitored from 4 to 80 or 120°C at a ramp rate of 1°C/min on a MicroCal VP-DSC microcalorimeter. A 1 s filtering period and high gain mode were used to check the transition temperature of all the bicelle preparations.

Thermal denaturation measurements of hVDAC2

Thermal denaturation of folded hVDAC2 in various bicelle conditions was carried out on a JASCO (Easton, MD) J-815 circular dichroism (CD) spectropolarimeter. Wavelength scans were obtained at 4°C using a quartz cuvette of 1 mm pathlength and acquisition settings of 0.5 nm data pitch, 100 nm/min scan speed, 1 s data integration time, and 1 nm bandwidth. Data were averaged over three accumulations. Thermal denaturation was monitored at 215 nm from 4 to 95°C at 1°C intervals, with 1°C/min ramp rate, 1 nm bandwidth, and 1 s data integration time. Each experiment was repeated two to three times with independent protein preparations to check for reproducibility. After correction for buffer (and empty bicelle) contribution, data were smoothed using the means-movement method. The fraction unfolded (f_U) data were calculated using the following formula:

$$f_U = (\theta_{Obs} - \theta_F)/(\theta_{UF} - \theta_F).$$

Here, θ_{Obs} is the observed molar ellipticity at 215 nm (ME_{215}) at a given temperature, and θ_F and θ_{UF} are the ME_{215} values for the folded protein at 4°C and unfolded protein at 95°C, respectively. All f_U data were fitted to a two-state equation for thermal denaturation (32) to derive the T_m (the midpoint of thermal denaturation) and ΔH_{app} (cooperativity of the unfolding transition; the enthalpy measured is an apparent value because the protein shows irreversible unfolding). Values obtained from two to three independent experiments were averaged to obtain the mean T_m and ΔH_{app} and the SD.

Isothermal unfolding kinetics of hVDAC2

Folded hVDAC2 in bicelles was subjected to isothermal unfolding with time, and the process was monitored using far-ultraviolet (UV) CD at 215 nm.

Data were acquired from 40 to 95°C at 2°C intervals using a 1 s data integration time, 1 s data pitch, and 1 nm bandwidth. The first (rapid) transition was fitted to a single exponential decay function using reported methods (30) to derive the rate of protein unfolding (k_U) in each q of all bicelle preparations. The natural logarithm values of the rates ($\ln k_U$) were plotted against 1000/T, where T is the temperature in K. The Arrhenius plot was fitted to a linear function to derive the activation energy (E_{act}) using the formula slope $= -E_{act}/R$, where R is the gas constant (1.987 cal K^{-1} mol^{-1}).

All-atom MD Simulations

The hVDAC2 structure was generated using iterative threading assembly refinement (I-TASSER) (33) and used as the input file for all the simulations. The alignment of hVDAC2 in the lipid membrane was generated using PyMOL v1.5.0.5 by superposing the I-TASSER-generated hVDAC2 structure onto the zebrafish VDAC2 structure (Protein Data Bank: 4BUM) obtained from the Orientation of Proteins in Membranes database (25). The Bilayer Builder tool in the CHARMM-GUI web server (34) was used to generate the assembled hVDAC2-lipid moiety and the input files required for simulation.

One hVDAC2 molecule was inserted into an assembled lipid bilayer that was generated with or without cholesterol (1). For the condition without cholesterol, four bilayer types were generated using PC lipids of varying hydrocarbon chain length, as follows: 1) 14-C, DMPC; 2) 16-C, DPPC; 3) 18-C, DSPC; and 4) equal mixture of DPPC and DSPC (2). For the condition with cholesterol, DPPC bilayers were generated with increasing cholesterol content (1.25, 5, 12.5, and 25% mole fraction cholesterol), corresponding to 1, 4, 10, and 20 cholesterol molecules per leaflet. Cholesterol was introduced in the bilayer by replacing the equivalent number of DPPC molecules.

In all cases, the protein-lipid complex was hydrated using a 2.0 nm water layer on either side of the bilayer, and 0.1 M NaCl was used to neutralize the charges. The final box dimension for each system was $8.5 \times 8.5 \times 8.5$ nm^3. A CHARMM-36 force field and NPT (constant particle number, pressure, and temperature) ensemble with zero external surface tension was used to generate the input assembly. The system contained one protein, 80 lipid molecules per leaflet, 19 Na^+ and 20 Cl^- ions, and ~9000–11,000 water molecules. In the DPPC/DSPC mixed bilayer system, an equal number of DPPC and DSPC molecules were retained in each leaflet. In the cholesterol-doped DPPC bilayer system, cholesterol molecules were distributed evenly in the upper and lower leaflets at the start of the simulation.

All simulations were carried out using GROMACS v5.0.4 (35) using reported methods (36). For systems without cholesterol, two 200 ns simulations were carried out using independent starting VDAC-lipid assemblies. For the DPPC-cholesterol assemblies, one 100 ns simulation was run using independent starting VDAC-lipid assemblies. The temperatures used for the final equilibration and production steps were maintained above the phase-transition temperature of each lipid (Table S1). For the mixed DPPC/DSPC system, the numerical average of the individual DPPC and DSPC phase-transition temperatures was used for the simulation. The temperature used for DPPC was retained for the DPPC-cholesterol system as well.

After energy minimization, six steps of equilibration were carried out, wherein restraints were reduced in a stepwise manner (37). At the end, a production run with zero restraints was executed to generate the final trajectory. Analysis of the trajectory was carried out using GROMACS v5.0.4, VMD v1.9.3, or PyMOL. GridMAT-MD_V2.0 or MEMBPLUGIN v1.1 (38) was used to calculate the average lipid thickness map, area per lipid (APL), and lipid order parameter (S_{cd}). Here, the lipid ordered parameter is defined as the angle of rotation of acyl chains from its bilayer normal axis and can be calculated using the formula (39)

$$S_{cd} = \langle 3\cos^2\theta - 1 \rangle / 2,$$

where θ is the angle between the C-H bond vector to the bilayer normal axis.

Data from the first 5 ns of the simulation was excluded for RMSF calculation. Lipid physical parameters including S_{cd}, APL, and bilayer thickness were calculated using 50 successive frames between 10 and 200 ns of the simulation data. The change in lipid thickness along the trajectory was calculated from the distance between center of mass of all the phosphate atoms present in the two lipid leaflets.

RESULTS AND DISCUSSION

Intrinsic protein-lipid interactions and protein adaptation can be studied biophysically by varying the protein/lipid ratios and lipid characteristics (e.g., headgroup, chain length, saturation). Here, we specifically address the effect of PC lipids, which are the most abundant OMM lipids, on hVDAC2. To deduce protein stability, we characterize hVDAC2 biophysically by measuring the protein response to temperature in PC and cholesterol-doped PC membranes. Further, we present all-atom MDSs results of hVDAC2 dynamics in PC and doped-PC bilayers. Our results show that an optimal negative mismatch imposed by the PC bilayer stabilizes the hVDAC2 β-barrel.

hVDAC2-*di*16:0-PC negative mismatch stabilizes the β-barrel

To address the effect of diacyl chain length on hVDAC2, we prepared isotropic PC bicelles of $q = 1.0$ in *di*C14:0-PC (DMPC), *di*C16:0-PC (DPPC), and *di*C18:0-PC (DSPC) as the long-chain lipid. Although the physical properties of bicelles are different from lipid bilayers (40), they are useful membrane mimetics that support the folding of hVDAC2. Of the three lipids, DPPC (~36%), DSPC (~20%), and the unsaturated analogs of DSPC (C18:1-PC, ~18%; C18:2-PC, ~16.6%) are abundant in the OMM, constituting >90% of the total PC content (41,42). We used DPC (monoacyl C12:0-PC (43)) as the short-chain lipid. The far-UV CD spectrum of hVDAC2 folded in bicelles shows a negative maximum at ~215 nm, which is characteristic of a β-rich structure. The spectra are similar in all three lipids (DMPC, DPPC, and DSPC) (Fig. 1 *A*, *left*, BM spectra), suggesting that β-barrel formation is supported in all three diacyl chain PCs. We additionally verified β-barrel formation using its fluorescence properties and ion-channel-gating characteristics (see Fig. S2).

We used temperature as the perturbant to monitor hVDAC2 stability. Upon heating, hVDAC2 undergoes coupled unfolding and aggregation (30,31). These aggregates contribute marginally to the measured ellipticity at 215 nm (Fig. 1 *A*, *left*, after melting [AM] spectra). Hence, the thermal denaturation monitored using far-UV CD measures the combined process of barrel unfolding and aggregation. We followed the unfolding and aggregation processes by monitoring the loss in secondary structure content (reduction in ellipticity at 215 nm) using far-UV

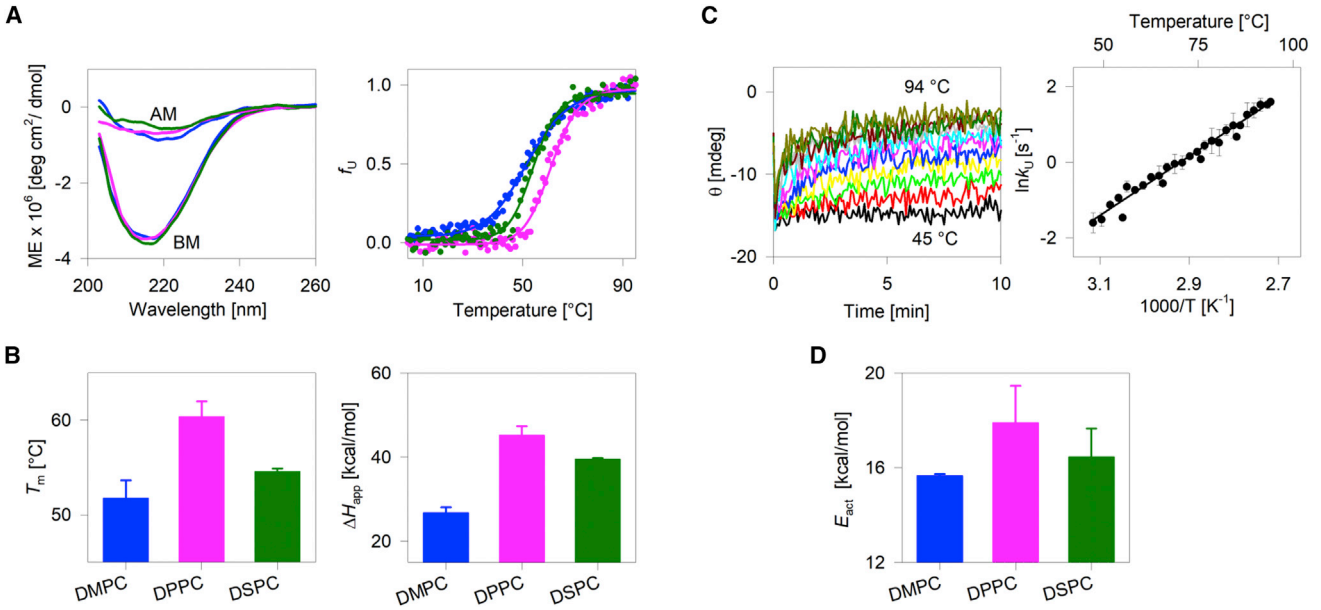

FIGURE 1 Effect of lipid-diacyl-chain length on hVDAC2 stability. (*A*, *left*) Representative far-UV CD wavelength scans of folded hVDAC2 at 4°C. BM, before thermal denaturation; AM, after thermal denaturation. (*A*, *right*) Dependence of the unfolded protein fraction (f_U) on temperature, derived from far-UV CD thermal unfolding at 215 nm. Fits of the data from DMPC (*blue*), DPPC (*pink*), and DSPC (*green*) bicelles to a two-state thermal denaturation model are in solid lines. (*B*) Comparison of the T_m and ΔH_{app} derived from the thermal unfolding measurements reveals that stability is highest in DPPC. Error bars represent the SD calculated from three independent experiments. The significance of the differences was measured for DMPC and DSPC with respect to DPPC using *t*-test. In the case of T_m, *p*-values are 0.0005 for DMPC-DPPC and 0.0012 for DSPC-DPPC. For ΔH_{app}, *p*-values are 0.0002 for DMPC-DPPC and 0.01 for DSPC-DPPC. (*C*, *left*) Representative isotherms for the unfolding kinetics of hVDAC2 monitored in DMPC using far-UV CD (215 nm) at various temperatures from 46 to 94°C at 2°C intervals. The fit of each isotherm to a single exponential function provided the unfolding rate (k_U) at that temperature. (*C*, *right*) A representative Arrhenius plot (in DMPC bicelles) obtained by plotting the ln k_U against temperature. Fit (*solid line*) of the data to the Arrhenius equation yielded the activation energy (E_{act}). (*D*) Dependence of E_{act} of hVDAC2 on the acyl-chain length. Error bars represent the SD calculated from two independent experiments, with each experiment containing ~25 independently measured rates. Overall, the hVDAC2 stability from T_m, ΔH_{app}, and E_{act} is highest in DPPC. The complete data are presented in Figs. S3 and S4. To see this figure in color, go online.

CD. The thermal transition of empty bicelles was assessed independently using microcalorimetry to ensure that the lipid phase transition temperature was different from protein unfolding (Fig. S3). We also verified that the transition temperature of our bicelle preparations matches previous reports (44).

Fig. 1 summarizes our results from thermal denaturation studies. hVDAC2 unfolds cooperatively beyond ~25–50°C in the different bicelle preparations (Fig. 1 *A*, *right*; Fig. S4). The data were fitted to a two-state thermal denaturation function using reported methods (32) to derive the midpoint temperature of unfolding and aggregation (T_m) and the apparent unfolding and aggregation enthalpy (ΔH_{app}; representing cooperativity of the unfolding process) in each lipid. Notably, DPPC, with a 16-C diacyl chain, emerges as the most thermostable lipidic condition for hVDAC2. Here, the two major measures of protein stability (T_m and ΔH_{app}) are significantly high only in DPPC (Fig. 1, *A* and *B*). DMPC, which has a 14-C diacyl chain, emerges as the lowest thermostable lipidic condition for hVDAC2, whereas the barrel exhibits moderate stability in DSPC. A nonlinear variation in hVDAC2 stability is therefore seen with a linear increase in diacyl PC chain length.

Additionally, we measured the activation energy barrier (E_{act}) separating the folded and aggregated states of hVDAC2. Here, the rate of hVDAC2 unfolding and aggregation is measured using far-UV CD by monitoring the rate of loss in θ_{215} at different temperatures (Fig. 1 *C*, *left*). The plot of the coupled unfolding and aggregation rate at specific temperatures correlates linearly with the temperature (Fig. 1 *C*, *right*), and the E_{act} is derived from the Arrhenius equation. In line with the thermal parameters, the E_{act} is also the highest in DPPC:DPC bicelles (Figs. 1 *D* and S4).

Interestingly, in DPPC bilayers, where hVDAC2 stability is highest, the β-barrel exhibits a negative mismatch to the hydrophobic bilayer (see Fig. S5). This is also evident when we compare the transmembrane domain span of VDACs (hydrophobic thickness of ~2.3 ± 0.11 nm (25–28)) with the physical properties of the DPPC bilayer. The diacyl chains of DPPC provide a hydrophobic span of ~2.9 nm. In contrast, the membrane span of the 14-C DMPC is ~2.6 nm (29). Although DMPC provides a better match to the hydrophobic face of hVDAC2, our experiments reveal that the barrel exhibits lowered stability in this lipid. Therefore, we find that a degree of specificity exists between hVDAC2 and

its surrounding lipid, with negative mismatch optimally stabilizing the barrel.

hVDAC2 structural rigidity highest in optimal negative mismatch provided by DPPC bilayer

To understand the molecular basis of hVDAC2 stability in bilayer mismatch conditions and to validate our conclusions, we carried out all-atom MDSs of hVDAC2 in PC bilayers. First, we modeled the structure of hVDAC2 based on the available structures of hVDAC1 and zebrafish VDAC2. The modeled β-barrel was then assembled in a lipid bilayer (~80 lipid molecules in each leaflet). The lipids used were *di*C14:0-PC (DMPC), *di*C16:0-PC (DPPC), *di*C18:0-PC (DSPC), and an equimolar mixture of *di*C16:0-PC and *di*C18:0-PC (DPPC-DSPC; DPDS). The protein-lipid assembly was first equilibrated by energy minimization. Each equilibrated assembly was used to perform independent 200 ns all-atom MDSs at a temperature that was at least 1°C above the reported phase transition temperature of the lipid (36).

Fig. 2, *A* and *B* compare the root mean-square deviation (RMSD), difference in per-residue root mean-square fluctuation (ΔRMSF), and total RMSF in DMPC (14-C), DPPC

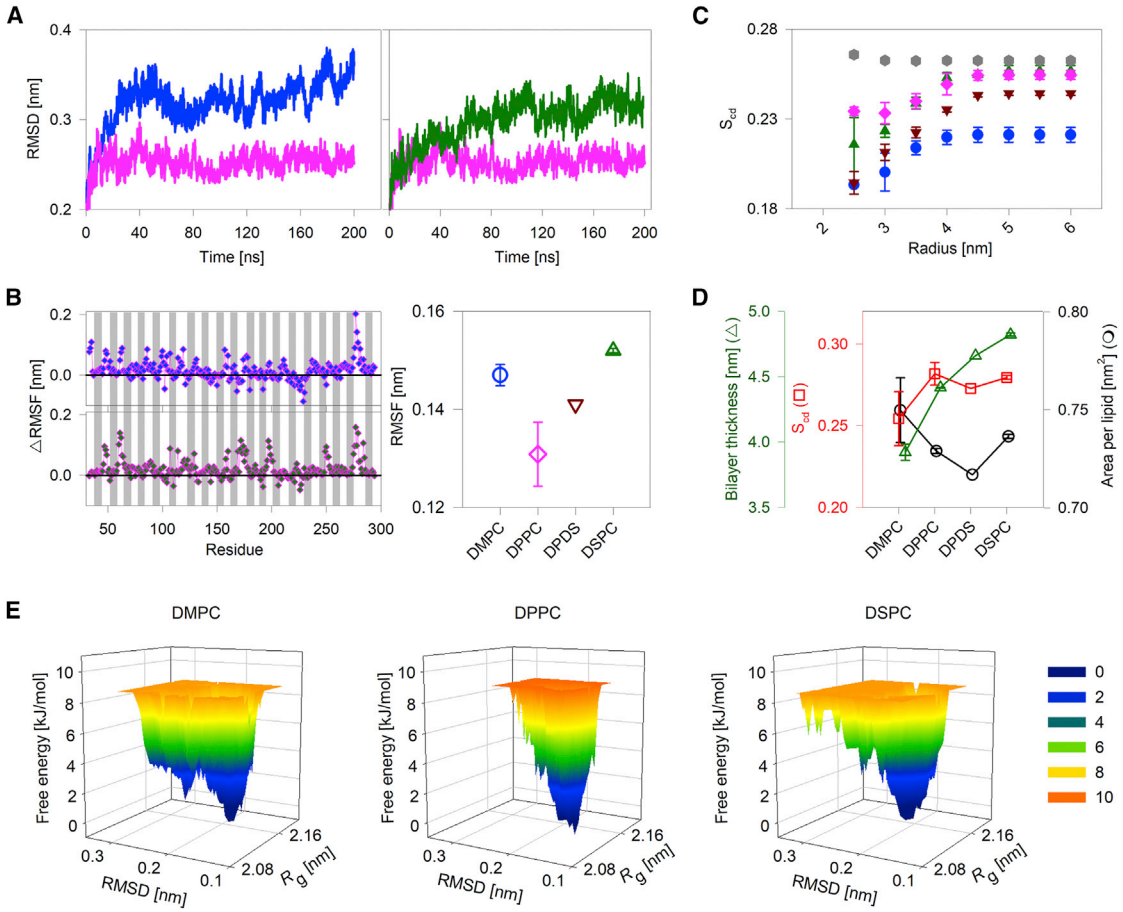

FIGURE 2 hVDAC2-lipid parameters derived from all-atom MDSs. (*A*) A comparison of the RMSD in DMPC (*blue*), DPPC (*pink*), and DSPC (*green*) for the transmembrane region of hVDAC2. The RMSD is lowest in DPPC. (*B*) A comparison of per-residue ΔRMSF (*left*) and overall RMSF of the transmembrane region (*right*) in PC bilayers. ΔRMSF was calculated for each residue as $RMSF_{DMPC} - RMSF_{DPPC}$ (*left*, *top*) and $RMSF_{DSPC} - RMSF_{DPPC}$ (*left*, *bottom*). The 19 β-strands are indicated by gray bars, and loop regions are shown as white spaces (α1 is omitted). Data for DPPC + DSPC (DPDS) is in brown. The RMSF is lowest in DPPC. (*C* and *D*) Variation in lipid physical properties such as bilayer order parameter (S_{cd}), area per lipid (APL), and bilayer thickness in the presence of hVDAC2. (*C*) Bilayer S_{cd} was calculated for 50 frames from 10 to 200 ns trajectory are plotted for each acyl carbon of DMPC (*blue circle*), DPPC (*pink diamond*), DSPC (*green upward triangle*), and DPDS (*brown inverted triangle*) protein-lipid bilayer systems. Also included as control is the S_{cd} for DPDS bilayer without protein (*gray hexagons*), wherein no change in the S_{cd} is seen. The magnitude of increase in S_{cd} is lowest in DPPC; DPPC also shows the highest S_{cd} near the protein. Also note that the presence of protein decreases the overall S_{cd} (compare *gray hexagons* with *brown inverted triangles* at 6 nm). (*D*) Average S_{cd}, APL, and bilayer thickness derived from 50 frames of the 10 to 200 ns trajectory for the four lipid conditions shows a nonlinear change in S_{cd}, APL, and bilayer thickness with a linear increase in the acyl-chain length. All error bars are from two independent 200 ns simulations. (*E*) A representative FEL plotted with respect to the radius of gyration (R_g) and RMSD of hVDAC2 in DMPC, DPPC, and DSPC bilayers. In DPPC, hVDAC2 samples a limited number of compact conformations (see the lower R_g values) and also lower RMSD values along the trajectory when compared to other lipids. Numbers beside the color scale correspond to the free energy in kJ/mol. A lower free-energy value corresponds to a more stable system. Additional data and analyses are presented in Figs. S5–S16. To see this figure in color, go online.

(16-C), and DSPC (18-C). Notably, these values are lowest in the DPPC system, which indicates that hVDAC2 is less dynamic in DPPC. The dynamicity is lowered for both the strand and loop residues (Fig. S6); therefore, DPPC modulates the RMSF of the complete hVDAC2 barrel. The values are high in both DMPC and DSPC, suggesting that the structural plasticity of hVDAC2 is modulated nonlinearly with changes in bilayer thickness. We reach a similar conclusion upon mapping the protein dynamics on hVDAC2 structure (see Figs. S7–S9).

The free-energy landscape (FEL) represents various conformational states present in a protein molecule. We plotted the FEL with respect to changes in the radius of gyration R_g (representing the compactness of a molecule; the lower the R_g, the greater the compactness) and RMSD (representing the overall structural deviation from the original structure). A narrow FEL with lower RMSD and R_g indicates that the complex samples a limited number of compact conformations along the trajectory and leads to the formation of a barrel that is buried. We obtain a narrow FEL only for the hVDAC2-DPPC system, suggesting that the system dynamicity is low here, and it attains an energy-minimized stable state. On the other hand, the FEL is high for DMPC and DSPC systems, suggesting increased dynamicity in the system. Overall, our observation from MDS is in excellent agreement with our experiments and confirms that hVDAC2-DPPC systems are optimally stabilized. The structural plasticity increases as the diacyl chain is either shortened to 14-C in DMPC or lengthened to 18-C in DSPC. We conclude that hVDAC2 barrel stability is modulated nonlinearly with bilayer thickness.

hVDAC2 dynamics depends on its lipid environment. In turn, the physical properties of the lipids can be affected in the presence of hVDAC2. Hence, we analyzed lipid alterations occurring because of the hVDAC2 molecule. We calculated the distance dependence of the lipid order parameter (S_{cd}) at 2.5–6.0 nm from the center of hVDAC2 pore using a 0.5 nm gap size. The analysis shows that the order parameter is lowered considerably near the protein, as it introduces perturbation in the lipid bilayer (Fig. 2 *C*). Notably, the S_{cd} at a distance >4.0 nm is still lower than the S_{cd} calculated from simulations of bilayers lacking protein (for example, the S_{cd} of DPDS at 6.0 nm is ~0.26 and ~0.24 without and with hVDAC2, respectively; Fig. 2 *C*). Therefore, the incorporation of hVDAC2 alters the physical properties of the PC bilayer.

Interestingly, the acyl-chain ordering in the protein vicinity is highest for DPPC. Further, the overall S_{cd}, APL, and bilayer thickness are expected to change linearly with 2-C increase in the acyl chain. However, we find that the lipid physical properties vary nonlinearly between DMPC, DPPC, and DSPC (Fig. 2 *D*), supporting our inference that the hVDAC2 barrel distinctively affects the bilayer characteristics. Additionally, in DPPC, in which hVDAC2 is stabilized by optimal negative mismatch, alteration of lipid physical properties is lowest. In other words, the hVDAC2 barrel is accommodated in DPPC with minimal changes in the local physical properties of the lipid molecules.

We also observe prominent membrane thinning in the vicinity of strands $\beta1$–$\beta3$, $\beta7$–$\beta9$, and $\beta17$–$\beta19$ in all lipidic conditions (see Figs. S10–S16). These strands comprise known homo- and hetero-oligomerization zones for VDACs (16,45,46), suggesting that intrinsic weakening of protein-lipid interactions, driven by increase in polarity of residues in the primary sequence, may facilitate VDAC association with its binding partners.

Bilayer physical properties influence hVDAC2-lipid interplay

Next, we asked whether it is the bilayer physical property that regulates hVDAC2 stability or whether our observation was specific to *di*16:0-PC. To address this, we used cholesterol. Cholesterol alters the physical properties and dynamics of the bilayer, such as bilayer thickness, fluidity, melting temperature of lipids and membrane microviscosity, and lipid bilayer packing (47). First, we folded the protein in DMPC, DPPC, and DSPC bicelles containing preincorporated cholesterol. We varied the cholesterol content from 0.02 to 0.04% (with respect to long-chain lipid); this corresponds to 13–26 mol% cholesterol for a bicelle of $q = 1.0$. The conditions of diacyl PC bicelles containing cholesterol wherein we were successfully able to fold hVDAC2 are listed in Table S2. DSPC bicelles with higher cholesterol content did not support the folding of hVDAC2, likely because of the increase in lipid ordering and negative mismatch. Hence, our results from cholesterol-doped DSPC are limited.

Fig. 3, *A* and *B* summarize our results from hVDAC2-PC-cholesterol systems. We obtain comparable far-UV CD spectra for hVDAC2 in the absence and presence of increasing cholesterol content in the PC membrane (Fig. 3 *A*, *left*). Further, cooperative unfolding and aggregation of hVDAC2 is observed in all conditions (Fig. 3 *A*, *right*; also Fig. S17). A comparison of the thermal parameters derived from the denaturation measurements show that increasing the cholesterol content has an overall destabilizing effect on hVDAC2 in cholesterol-doped DPPC bicelles (Fig. 3 *B*). Largely, the T_m is lowered as the cholesterol doping increases. Also interesting is to note that with increasing cholesterol content, hVDAC2 T_m increases in DMPC bicelles (Fig. 3 *B*, *left*). This observation contrasts with the results we obtained for nondoped conditions (see Fig. 1). The ΔH_{app} is largely similar in all conditions, suggesting that cholesterol primarily influences the stability of only the folded state of hVDAC2.

Cholesterol increases bilayer thickness by increasing acyl chain ordering (47). Our results (Fig. 3, *A* and *B*) allow us to conclude that the bilayer thickness, which is modulated by cholesterol, regulates the stability of folded hVDAC2.

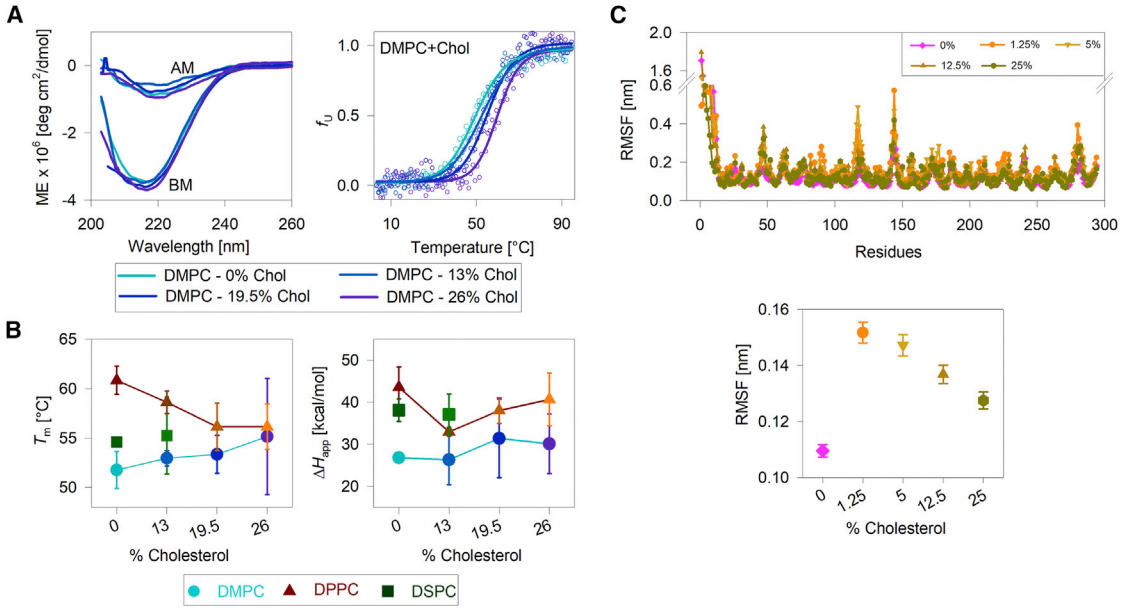

FIGURE 3 Effect of bilayer thickness and acyl-chain ordering on hVDAC2 stability. (*A*, *left*) Representative far-UV CD wavelength scans of folded hVDAC2 at 4°C in DMPC bicelles doped with increasing mole percent of cholesterol (0–26%). BM, before thermal denaturation; AM, after thermal denaturation. (*A*, *right*) Dependence of the unfolded protein fraction (f_U) on temperature, derived from far-UV CD thermal unfolding at 215 nm (see *foot* of the figure for *color code*). Fits of the data to a two-state thermal denaturation model to derive T_m and ΔH_{app} are in solid lines. Increasing the cholesterol content increases hVDAC2 thermal stability in DMPC bicelles. (*B*) A comparison of the T_m and ΔH_{app} derived in all three bicelles with and without cholesterol (see *foot* of the figure for color/symbol code). With increasing cholesterol content, the T_m increases in DMPC and decreases in DPPC. The ΔH_{app} shows a modest nonlinear variation with increasing cholesterol content, suggesting that the PC lipid modulates hVDAC2 stability without affecting the unfolding cooperativity. Error bars represent the SD from two to three independent experiments. For 26% cholesterol samples, errors in T_m are high because of difficulties in bicelle preparation. DSPC bicelles containing >13% cholesterol could not be prepared. (*C*) A comparison of per-residue RMSF (*top*) and overall RMSF (*bottom*) of the transmembrane region of hVDAC2 in DPPC bilayers doped with increasing mole percent of cholesterol. The RMSF is lowest in DPPC without additional cholesterol. Note that the % cholesterol in (*B*) and (*C*) cannot be compared directly because they represent mole percent in (*B*), obtained with respect to the concentration of the long-chain lipid, and mole fraction in (*C*). See Materials and Methods and Table S2 for details. The complete data and additional results are presented in Figs. S17–S26. To see this figure in color, go online.

Moreover, cholesterol-induced changes in protein stability is dependent on the acyl-chain length, suggesting that the optimal negative mismatch and membrane rigidity are foremost contributing factors to hVDAC2 stability. We reach a similar conclusion from our MDS results from hVDAC2-DPPC-cholesterol systems, wherein barrel dynamicity is lowest in 0% cholesterol (Figs. 3 *C* and S18–S26). We conclude that bilayer physical characteristics influence hVDAC2 stability, which can be varied through lipid-cholesterol interactions. It is also noteworthy that the vicinities of β7–β9 and β16–β18 retain the ability to cause bilayer thinning in cholesterol systems, reaffirming our inference that the lipid distribution is unaffected in this region of hVDAC2.

CONCLUSIONS

It is estimated that ~40–55% of the total OMM lipids are PCs (41,42), with 16:0-PC accounting for >35% and 18:0-PC for ~20% of the total OMM PC content (41). Further, VDACs are the most abundant OMM proteins. Hence, VDACs reside in a physiological environment rich in 16:0-PC and 18:0-PC. Our studies show that this negative mismatch provided by the OMM PCs indeed stabilizes hVDAC2. Although transmembrane helices adapt to the hydrophobic mismatch through conformational changes (9,10,48), bacterial transmembrane β-barrels are considered as rigid bodies that undergo structural deformation only under excessive mismatch or extreme lateral pressure (9,49). For example, *E. coli* OmpF binding to *di*(C14:1)PC is highest owing to the intrinsic hydrophobic match, and OmpF distorts bilayers of longer chains to achieve the hydrophobic matching (9). In interesting contrast, our study reveals that mitochondrial hVDAC2 is both sensitive to incremental changes in the diacyl-chain length and modulates its stability under conditions of bilayer match versus mismatch (Fig. 4). This biophysical response appears to be linked directly to the physical characteristics of the bilayer. Additionally, we find that unlike bacterial transmembrane β-barrels that exhibit characteristics of rigid structures (9), the hVDAC2 barrel undergoes deformation in all lipid-chain lengths; the scaffold deformation is lowest in DPPC. Hence, hVDAC2 is likely to be less rigid than its counterparts in the bacterial outer membrane.

Because mammalian mitochondria possess 16-C and 18-C PC lipids (42), we propose, based on our findings, that optimal mismatch conditions induced by PC chain length promotes hVDAC2 stability. Intraprotein and

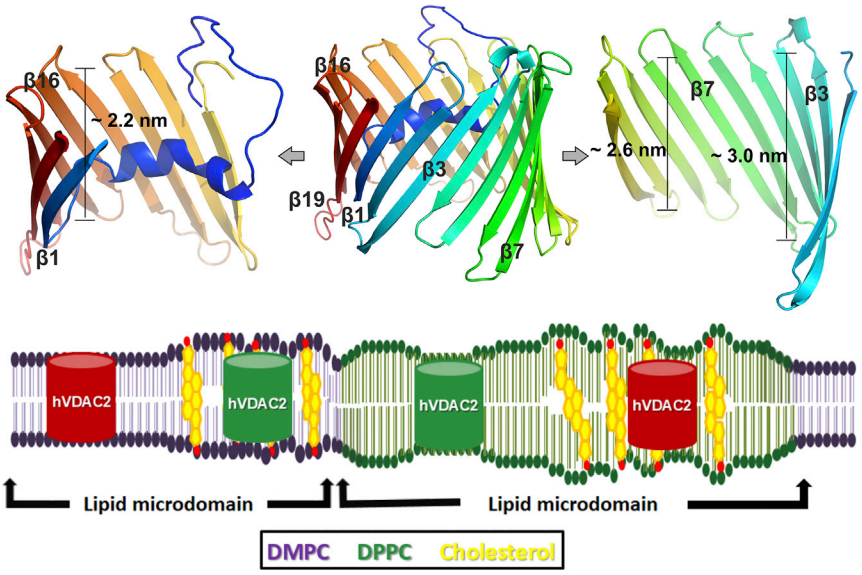

FIGURE 4 Interaction dynamics of the asymmetric scaffold of hVDAC2 barrel with physical properties of the surrounding bilayer. (*Upper panel*) A ribbon diagram highlighting the asymmetric scaffold of the hVDAC2 barrel. The complete barrel is shown in the middle. Strands $\beta2$–$\beta6$ (*right*) at the N-terminal region of hVDAC2 have a transmembrane span of ~3.0 nm, which decreases to ~2.6 nm at the middle of the barrel near $\beta9$–$\beta12$. Strands $\beta14$–$\beta18$ at the C-terminal region of hVDAC2 (*left*) have a dimension of ~2.2 nm and are expected to exhibit the highest negative mismatch with DPPC. Note that the N-helix docks in the vicinity of these strands and can contribute to the stability of the C-terminal region. (*Lower panel*) A cartoon representation of how hVDAC2 stability can be modulated by bilayer mismatch in various lipid microdomains in the presence of cholesterol. An optimal bilayer mismatch achieved with DMPC-cholesterol or DPPC bilayers can increase hVDAC2 stability (*green barrel*). Suboptimal mismatch may lower hVDAC2 stability (*red barrel*) and can modulate barrel oligomerization in the mitochondrial outer membrane. To see this figure in color, go online.

protein-lipid interactions, which are highest in DPPC membranes (see Figs. 1 and 2), along with asymmetry in the transmembrane region of the hVDAC2 barrel scaffold (Fig. 4, *upper panel*), could be important contributors to its measured stability in 16-C membranes. The ability of VDACs to induce local membrane deformation and thinning, as well as reduction in total lipid number in the vicinity of $\beta7$–9 and $\beta17$–$\beta19$-$\beta1$–$\beta3$ in all PCs (see Figs. S10 and S11), suggests that VDAC oligomerization interfaces are intrinsically available in the hVDAC2 barrel. Indeed, $\beta7$–$\beta10$ is a known zone for BAK (Bcl-2 homologous antagonist killer) binding (16) and VDAC oligomerization (11,50); the second zone ($\beta17$–$\beta19$, $\beta1$–$\beta3$) is needed for homodimer formation (28,51).

It is conceivable that mitochondria might be able to elegantly regulate VDAC stability and function by varying the generic bilayer physical properties. To our knowledge, this is the first observation of a negative mismatch stabilizing a human membrane protein barrel. Further studies in this direction could provide molecular insight on whether lipid sorting in the OMM allows VDACs to switch between homeostasis and apoptotic states.

SUPPORTING MATERIAL

Supporting Materials and Methods, 26 figures, and two tables are available at http://www.biophysj.org/biophysj/supplemental/S0006-3495(18)31220-7.

AUTHOR CONTRIBUTIONS

R.M. designed the research. S.R.S. and P.Z. performed the stability measurements. S.R.S. performed the simulations. All authors analyzed the data and wrote the manuscript.

ACKNOWLEDGMENTS

We thank Udit Aswal and Svetlana Maurya for technical assistance with the MDS.

S.R.S thanks IISER Bhopal for research fellowship. R.M. is a Wellcome Trust-DBT India Alliance Intermediate Fellow. This work was supported by the Wellcome Trust-DBT India Alliance award number IA/I/14/1/501305 to R.M.

REFERENCES

1. Schuler, M. H., F. Di Bartolomeo, …, T. Becker. 2015. Phosphatidylcholine affects the role of the sorting and assembly machinery in the biogenesis of mitochondrial β-barrel proteins. *J. Biol. Chem.* 290:26523–26532.
2. Laganowsky, A., E. Reading, …, C. V. Robinson. 2014. Membrane proteins bind lipids selectively to modulate their structure and function. *Nature.* 510:172–175.
3. Lee, A. G. 2011. Lipid-protein interactions. *Biochem. Soc. Trans.* 39:761–766.
4. Lee, A. G. 2011. Biological membranes: the importance of molecular detail. *Trends Biochem. Sci.* 36:493–500.
5. Andersen, O. S., and R. E. Koeppe, II. 2007. Bilayer thickness and membrane protein function: an energetic perspective. *Annu. Rev. Biophys. Biomol. Struct.* 36:107–130.
6. Nicolson, G. L. 2014. The fluid-mosaic model of membrane structure: still relevant to understanding the structure, function and dynamics of biological membranes after more than 40 years. *Biochim. Biophys. Acta.* 1838:1451–1466.
7. Ferrer, I. 2009. Altered mitochondria, energy metabolism, voltage-dependent anion channel, and lipid rafts converge to exhaust neurons in Alzheimer's disease. *J. Bioenerg. Biomembr.* 41:425–431.
8. Halbleib, K., K. Pesek, …, R. Ernst. 2017. Activation of the unfolded protein response by lipid bilayer stress. *Mol. Cell.* 67:673–684.e8.
9. O'Keeffe, A. H., J. M. East, and A. G. Lee. 2000. Selectivity in lipid binding to the bacterial outer membrane protein OmpF. *Biophys. J.* 79:2066–2074.

10. Lee, A. G. 2004. How lipids affect the activities of integral membrane proteins. *Biochim. Biophys. Acta.* 1666:62–87.
11. Messina, A., S. Reina, …, V. De Pinto. 2012. VDAC isoforms in mammals. *Biochim. Biophys. Acta.* 1818:1466–1476.
12. Zachariae, U., R. Schneider, …, A. Lange. 2012. β-Barrel mobility underlies closure of the voltage-dependent anion channel. *Structure.* 20:1540–1549.
13. Maurya, S. R., and R. Mahalakshmi. 2017. Mitochondrial VDAC2 and cell homeostasis: highlighting hidden structural features and unique functionalities. *Biol. Rev. Camb. Philos. Soc.* 92:1843–1858.
14. Smilansky, A., L. Dangoor, …, V. Shoshan-Barmatz. 2015. The voltage-dependent anion channel 1 mediates amyloid β toxicity and represents a potential target for Alzheimer disease therapy. *J. Biol. Chem.* 290:30670–30683.
15. Naghdi, S., and G. Hajnóczky. 2016. VDAC2-specific cellular functions and the underlying structure. *Biochim. Biophys. Acta.* 1863:2503–2514.
16. Naghdi, S., P. Várnai, and G. Hajnóczky. 2015. Motifs of VDAC2 required for mitochondrial Bak import and tBid-induced apoptosis. *Proc. Natl. Acad. Sci. USA.* 112:E5590–E5599.
17. Maurya, S. R., and R. Mahalakshmi. 2016. VDAC-2: mitochondrial outer membrane regulator masquerading as a channel? *FEBS J.* 283:1831–1836.
18. Weiser, B. P., R. Salari, …, G. Brannigan. 2014. Computational investigation of cholesterol binding sites on mitochondrial VDAC. *J. Phys. Chem. B.* 118:9852–9860.
19. Gattin, Z., R. Schneider, …, A. Lange. 2015. Solid-state NMR, electrophysiology and molecular dynamics characterization of human VDAC2. *J. Biomol. NMR.* 61:311–320.
20. Budelier, M. M., W. W. L. Cheng, …, A. S. Evers. 2017. Photoaffinity labeling with cholesterol analogues precisely maps a cholesterol-binding site in voltage-dependent anion channel-1. *J. Biol. Chem.* 292:9294–9304.
21. Rostovtseva, T. K., N. Kazemi, …, S. M. Bezrukov. 2006. Voltage gating of VDAC is regulated by nonlamellar lipids of mitochondrial membranes. *J. Biol. Chem.* 281:37496–37506.
22. Rostovtseva, T. K., and S. M. Bezrukov. 2008. VDAC regulation: role of cytosolic proteins and mitochondrial lipids. *J. Bioenerg. Biomembr.* 40:163–170.
23. Betaneli, V., E. P. Petrov, and P. Schwille. 2012. The role of lipids in VDAC oligomerization. *Biophys. J.* 102:523–531.
24. Eddy, M. T., T. C. Ong, …, R. G. Griffin. 2012. Lipid dynamics and protein-lipid interactions in 2D crystals formed with the β-barrel integral membrane protein VDAC1. *J. Am. Chem. Soc.* 134:6375–6387.
25. Lomize, M. A., A. L. Lomize, …, H. I. Mosberg. 2006. OPM: orientations of proteins in membranes database. *Bioinformatics.* 22:623–625.
26. Hiller, S., R. G. Garces, …, G. Wagner. 2008. Solution structure of the integral human membrane protein VDAC-1 in detergent micelles. *Science.* 321:1206–1210.
27. Ujwal, R., D. Cascio, …, J. Abramson. 2008. The crystal structure of mouse VDAC1 at 2.3 A resolution reveals mechanistic insights into metabolite gating. *Proc. Natl. Acad. Sci. USA.* 105:17742–17747.
28. Schredelseker, J., A. Paz, …, J. Abramson. 2014. High resolution structure and double electron-electron resonance of the zebrafish voltage-dependent anion channel 2 reveal an oligomeric population. *J. Biol. Chem.* 289:12566–12577.
29. Kučerka, N., M. P. Nieh, and J. Katsaras. 2011. Fluid phase lipid areas and bilayer thicknesses of commonly used phosphatidylcholines as a function of temperature. *Biochim. Biophys. Acta.* 1808:2761–2771.
30. Maurya, S. R., and R. Mahalakshmi. 2013. Modulation of human mitochondrial voltage-dependent anion channel 2 (hVDAC-2) structural stability by cysteine-assisted barrel-lipid interactions. *J. Biol. Chem.* 288:25584–25592.
31. Maurya, S. R., and R. Mahalakshmi. 2015. N-helix and cysteines interregulate human mitochondrial VDAC-2 function and biochemistry. *J. Biol. Chem.* 290:30240–30252.
32. Greenfield, N. J. 2006. Using circular dichroism spectra to estimate protein secondary structure. *Nat. Protoc.* 1:2876–2890.
33. Roy, A., A. Kucukural, and Y. Zhang. 2010. I-TASSER: a unified platform for automated protein structure and function prediction. *Nat. Protoc.* 5:725–738.
34. Jo, S., T. Kim, …, W. Im. 2008. CHARMM-GUI: a web-based graphical user interface for CHARMM. *J. Comput. Chem.* 29:1859–1865.
35. Van Der Spoel, D., E. Lindahl, …, H. J. Berendsen. 2005. GROMACS: fast, flexible, and free. *J. Comput. Chem.* 26:1701–1718.
36. Lee, J., X. Cheng, …, W. Im. 2016. CHARMM-GUI input generator for NAMD, GROMACS, AMBER, OpenMM, and CHARMM/OpenMM simulations using the CHARMM36 additive force field. *J. Chem. Theory Comput.* 12:405–413.
37. Cheng, X., S. Jo, …, W. Im. 2013. CHARMM-GUI micelle builder for pure/mixed micelle and protein/micelle complex systems. *J. Chem. Inf. Model.* 53:2171–2180.
38. Guixà-González, R., I. Rodriguez-Espigares, …, J. Selent. 2014. MEMBPLUGIN: studying membrane complexity in VMD. *Bioinformatics.* 30:1478–1480.
39. Heller, H., M. Schaefer, and K. Schulten. 1993. Molecular-dynamics simulation of a bilayer of 200 lipids in the gel and in the liquid-crystal phases. *J. Phys. Chem.* 97:8343–8360.
40. Caldwell, T. A., S. Baoukina, …, L. Columbus. 2018. Low- q bicelles are mixed micelles. *J. Phys. Chem. Lett.* 9:4469–4473.
41. Ardail, D., J. P. Privat, …, P. Louisot. 1990. Mitochondrial contact sites. Lipid composition and dynamics. *J. Biol. Chem.* 265:18797–18802.
42. Horvath, S. E., and G. Daum. 2013. Lipids of mitochondria. *Prog. Lipid Res.* 52:590–614.
43. Chaturvedi, D., and R. Mahalakshmi. 2018. Position-specific contribution of interface tryptophans on membrane protein energetics. *Biochim. Biophys. Acta Biomembr.* 1860:451–457.
44. Silvius, J. R. 1982. Thermotropic phase transitions of pure lipids in model membranes and their modifications by membrane proteins. *In* Lipid-Protein Interactions. P. C. Jost and O. H. Griffith, eds. John Wiley & Sons, Inc., pp. 239–281.
45. Geula, S., H. Naveed, …, V. Shoshan-Barmatz. 2012. Structure-based analysis of VDAC1 protein: defining oligomer contact sites. *J. Biol. Chem.* 287:2179–2190.
46. Maurya, S. R., and R. Mahalakshmi. 2016. Control of human VDAC-2 scaffold dynamics by interfacial tryptophans is position specific. *Biochim. Biophys. Acta.* 1858:2993–3004.
47. Chiu, S. W., E. Jakobsson, …, H. L. Scott. 2002. Cholesterol-induced modifications in lipid bilayers: a simulation study. *Biophys. J.* 83:1842–1853.
48. Kaiser, H. J., A. Orłowski, …, K. Simons. 2011. Lateral sorting in model membranes by cholesterol-mediated hydrophobic matching. *Proc. Natl. Acad. Sci. USA.* 108:16628–16633.
49. Hong, H., and L. K. Tamm. 2004. Elastic coupling of integral membrane protein stability to lipid bilayer forces. *Proc. Natl. Acad. Sci. USA.* 101:4065–4070.
50. Lella, M., and R. Mahalakshmi. 2018. Direct structural annotation of membrane protein aggregation loci using peptide-based reverse mapping. *J. Phys. Chem. Lett.* 9:2967–2971.
51. Hosaka, T., M. Okazaki, …, M. Shirouzu. 2017. Crystal structural characterization reveals novel oligomeric interactions of human voltage-dependent anion channel 1. *Protein Sci.* 26:1749–1758.

Biophysical Journal, Volume *115*

Supplemental Information

Hydrophobic Mismatch Modulates Stability and Plasticity of Human Mitochondrial VDAC2

Shashank Ranjan Srivastava, Punit Zadafiya, and Radhakrishnan Mahalakshmi

SUPPORTING METHODS

Indirect folding in phosphocholine bicelles

Folding of hVDAC2 in 20 mM DPC micelles was initiated by 10-fold dilution of the unfolded protein stock in DPC micelles prepared in buffer A containing 10 mM DTT, at 4 °C. The sample was gently mixed for 5-6 h at 4 °C and trace amounts of aggregated protein was removed by centrifugation. The final folded protein concentration in 20 mM DPC micelles was 50 μM. This served as the 10X folded protein-DPC stock. Empty bicelles of various q in 0.9 volume buffer A were prepared by mixing specific stock concentrations (to achieve 4 mM final concentrations) of the long chain lipid with 2 mM (final concentration) DPC. The mixture was subjected to repeated freeze-thaw cycles using liquid nitrogen and heating, till the solution became transparent. The bicelles were chilled on ice, and 0.1 volume of the folded protein-DPC stock was diluted 10-fold in the bicelle preparation. This provided final concentrations of 5 μM protein, 4 mM DPC and 4 mM long chain lipid (bicelle q = 1.0), in buffer A containing 2 mM DTT. The reconstituted bicelles were subjected to three rounds of heating (35 °C) – cooling (4 °C) – vortexing (30 s) cycles and then allowed to equilibrate overnight at 4 °C by gentle mixing at 15 rpm. Trace amounts of aggregated protein was removed by centrifugation.

SUPPORTING TABLES

Table S1. Temperatures used for simulation according to the lipid system

Lipid	Phase transition temperature	Temperature for simulations	Thickness (hydrocarbon region)[@]	Thickness (bilayer)[@]
DMPC	24 °C	25 °C (298 K)	~25.7 Å	~37.0 Å
DPPC	41 °C	42 °C (315 K)	~28.5 Å	~40.0 Å
DSPC	55 °C	56 °C (329 K)	~32.0 Å	~43.0 Å
DPPC/DSPC	-	47.5 °C (320.5 K) [#]		
Cholesterol + DPPC	-	42 °C (315 K)		

[#]Numerical average of the phase transition temperatures of DPPC and DSPC was used.
[@]Obtained from Ref. (1).

Table S2. Cholesterol-doped lipidic bicelles.

Bicelle	% Cholesterol[#,$]		
	0.02%	**0.03%**	**0.04%**
DMPC/DPC	1.0	1.0	1.0
DPPC/DPC	1.0	1.0	1.0
DSPC/DPC	1.0	–	–

[#]Bicelle *q* that could be prepared is indicated.
[$]Cholesterol percentage calculation: The number of moles of the long chain lipid for $q = 1$ was first derived. The number of moles of cholesterol that would constitute x% was then calculated, with respect to mole amounts of the long chain lipid. This was then converted to milligram amounts of cholesterol to be added in the solution. This milligram amount was represented as percent w/v of cholesterol in the final solution.

SUPPORTING FIGURES

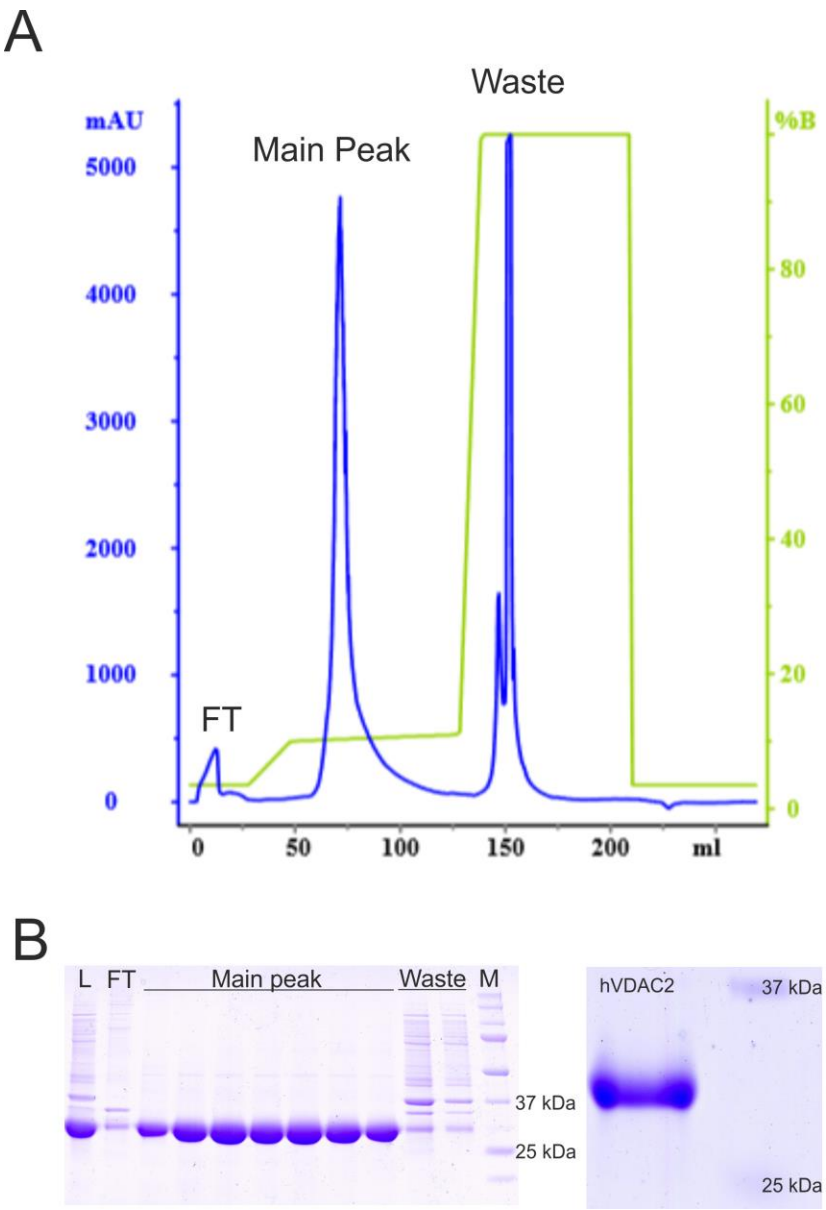

Figure S1. hVDAC2 purification. (A) Representative denaturing fast protein liquid chromatography (FPLC) purification profile of hVDAC2 obtained on a 20 ml HiPrep Q-FF column (GE Healthcare) using Buffer A (20 mM Tris-HCl pH 9.5 containing 8M urea) and Buffer B (Buffer A + 1 M NaCl). Absorbance recorded at 280 nm (blue) and the NaCl concentration gradient (green) are indicated. hVDAC2 eluted at 10-11% NaCl (main peak). (B, left) 12% SDS-PAGE gel showing protein contents of various fractions (L: load; FT: unbound flow through; Waste: tightly bound fraction; M: molecular weight marker). (B, right) Representative 12% SDS-PAGE image of purified hVDAC2 used for various experiments on the left lane with the molecular weight marker on the right. The expected MW of hVDAC2 is ~31.5 kDa.

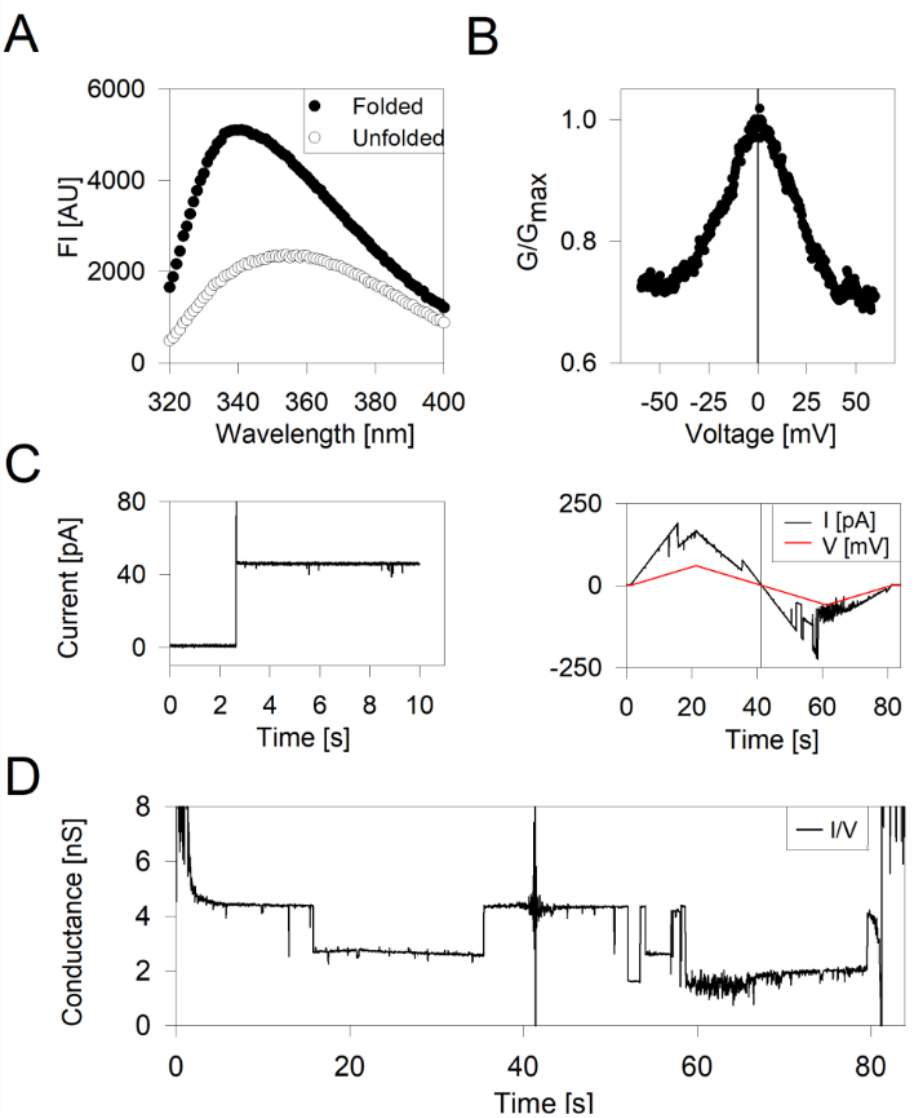

Figure S2. Characterization of folded hVDAC2. (A) Representative of tryptophan fluorescence emission spectra of folded hVDAC2 (filled black circles) and unfolded spectra (open circles) in bicelles obtained at low and high GdnHCl concentrations, respectively. The fluorescence intensity (FI) of folded hVDAC2 is high and shows a prominent blue shift when compared to unfolded hVDAC2. This data suggests that hVDAC2 is folding properly in bicelles. (B-D) Electrophysiology measurements of hVDAC2 folded in lauryldimethylamine oxide micelles and inserted in a single DiPhPC bilayer membrane containing 0.1% cholesterol (2, 3). (B) G/G_{max} plot shown for hVDAC2 protein obtained in response to a voltage gradient ranging from +60 to -60 mV is characteristic of a functional hVDAC molecule. (C, left) Single channel insertion at 10 mV produces a current of ~40 pA for the open state of hVDAC2 (2, 3). (C, right) The corresponding current measured for a voltage ramp program run from +60 mV to –60 mV with a 3mV/s ramp rate is shown. (D) Single channel conductance obtained by calculating I/V. A typical channel behavior characteristic of functional VDAC is obtained, confirming that the protein is well folded and functional in the bilayer.

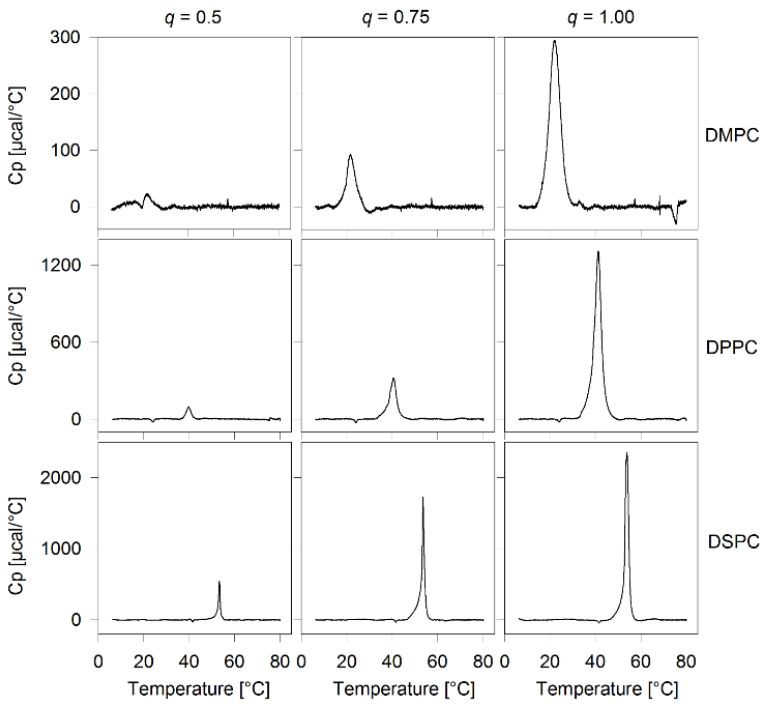

Figure S3. Comparison of bicelle phase transition temperatures using DSC. The phase transition temperature (T_m) of different lipidic bicelles (DMPC/DPC, DPPC/DPC, and DSPC/DPC) of various q was derived using differential scanning microcalorimetry (DSC). The phase transition temperature (T_m) is in excellent agreement with reported values for lipidic bicelles (4). The observation of a single transition represents homogeneous population of bicelles in all preparations.

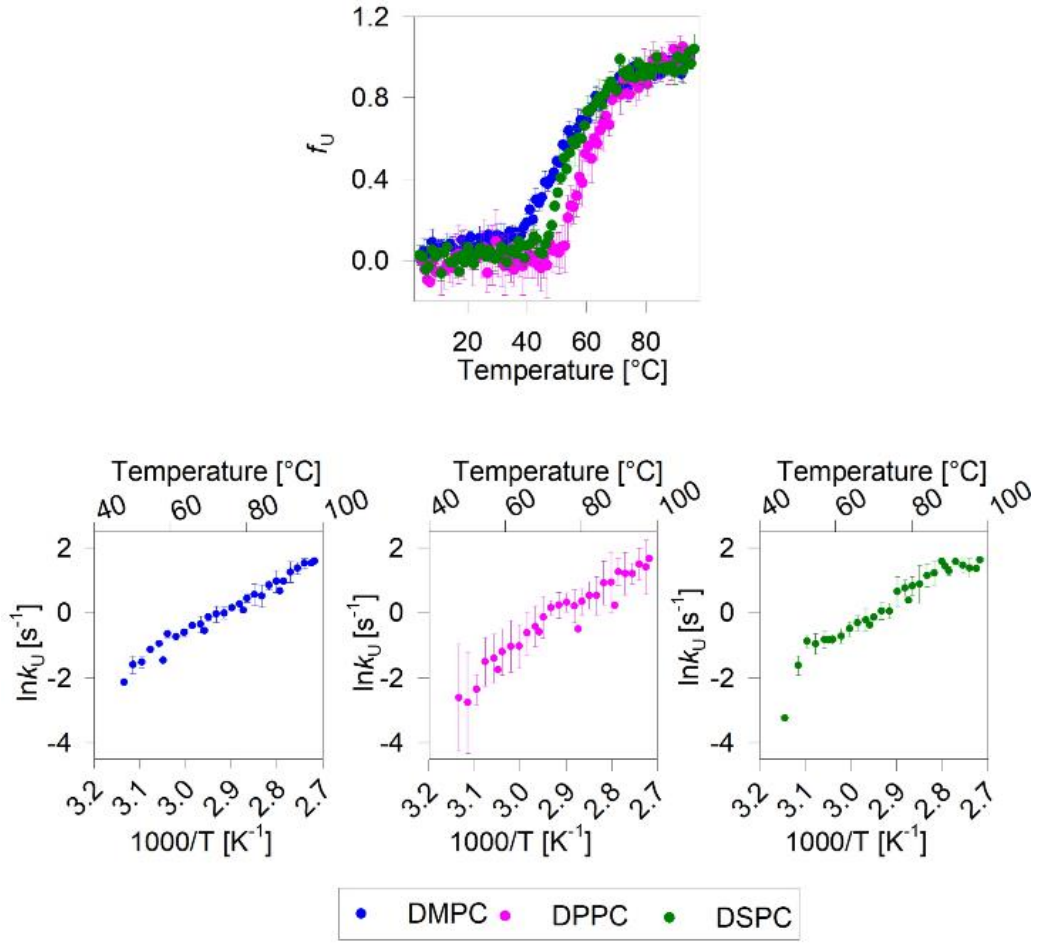

Figure S4. Effect of lipid chain length on the thermal stability of hVDAC2. (Top) Dependence of the unfolded protein fraction (f_U) on temperature, derived from far-UV CD thermal unfolding at 215 nm. Plot shows the normalized CD data obtained from q = 1.00 DMPC/DPC (blue), DPPC/DPC (pink) and DSPC/DPC (green) bicelle conditions. Error bars represent the s. d. calculated from 3-5 independent experiments. The thermal parameters presented in Figure 2B were derived from fits of individual data to the two-state thermal denaturation model. (Bottom panel) Unfolding rates (k_U) derived from fits of the isothermal unfolding kinetics to a single exponential function. Shown here is the Arrhenius plot for q = 1.0 bicelles in all three lipidic conditions. Error bars represent the s. d. calculated from 2-3 independent experiments. Activation energy (E_{act}) calculation was done by fitting the linear zone of the unfolding rates to the Arrhenius equation. Data in the regions below ~50 °C and above ~90 °C were not included in the fitting. The E_{act} presented in Figure 2D was calculated by fitting individual datasets (and not the mean data) to the Arrhenius equation. The error bars shown in Figure 2D therefore represent the s. d. obtained from the independent datasets. The k_U data clearly indicate that there are only marginal differences in E_{act} across the three lipid conditions. Color guide for both the plots is shown below the plot.

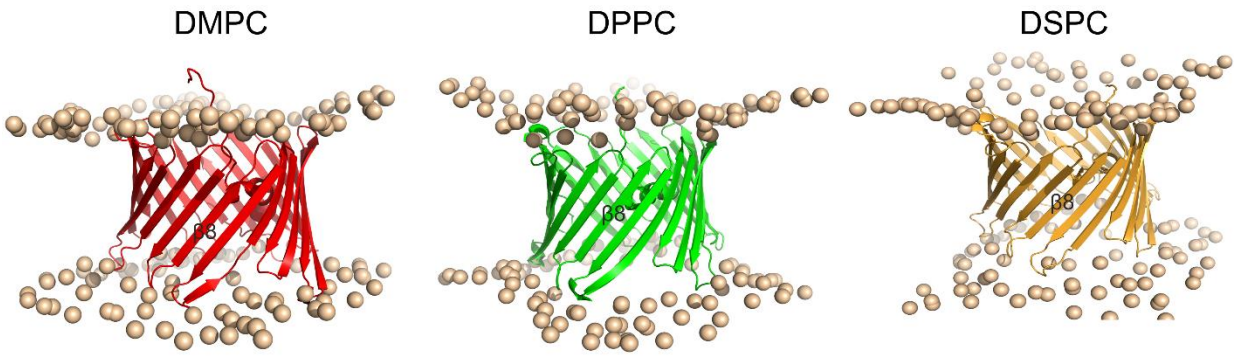

Figure S5. Increasing diacyl PC chain length increases the negative mismatch on the hVDAC2 barrel. Ribbon diagrams representing the average simulated assembly of hVDAC2 in PC lipids of varying chain length DMPC (*di*14:0-PC) (left), DPPC (*di*16:0-PC) (middle), and DSPC (*di*18:0-PC) (right). Wheat color spheres represent phosphate atom of the lipid head group. DMPC shows an excellent match to the hVDAC2 barrel, while the DSPC bilayer shows the highest negative mismatch with hVDAC2 barrel; DPPC lies between DMPC and DSPC. The barrel structure is colored based on the protein stability (deduced from experimental measurements and from barrel plasticity values obtained from MDS), with the most favorable condition represented in green and the least favorable condition represented in red. Of the three lipid conditions, DPPC provides optimal negative mismatch that stabilizes hVDAC2 barrel.

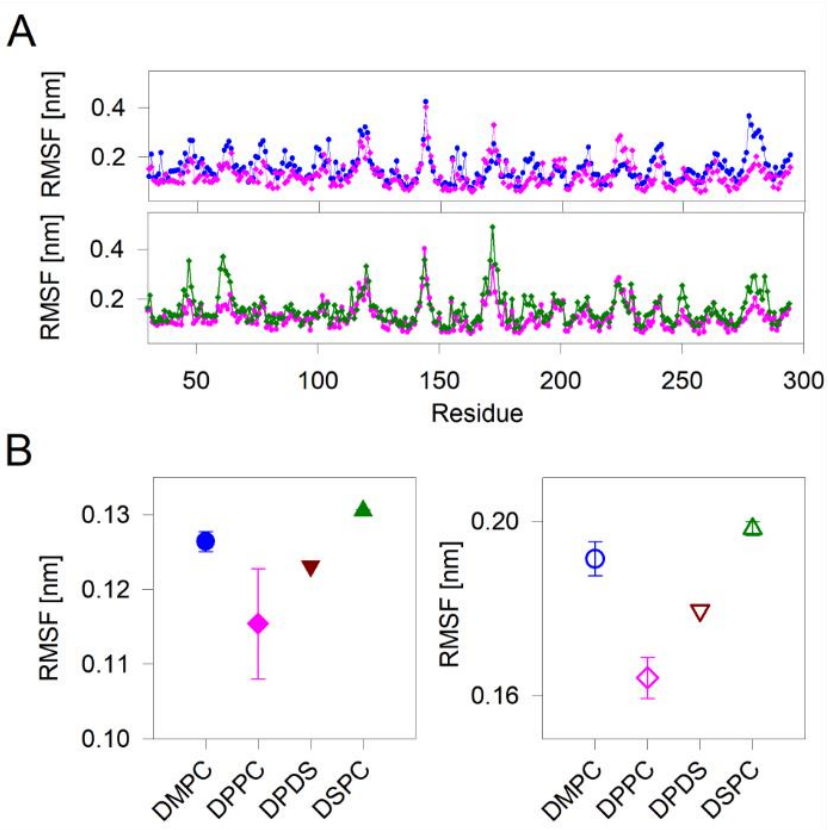

Figure S6. hVDAC2 RMSF in various lipid conditions. (A) Comparison of per-residue RMSF by overlaying DMPC–DPPC system (upper panel) and DPPC–DSPC system (lower panel). Color codes used are: DMPC in blue, DPPC in pink and DSPC in green. (B) Average per residue RMSF for the strand residue (left) and for the loop residue (right) is shown (DPDS is in brown). Error bar represents standard deviation of two independent 200 ns simulations.

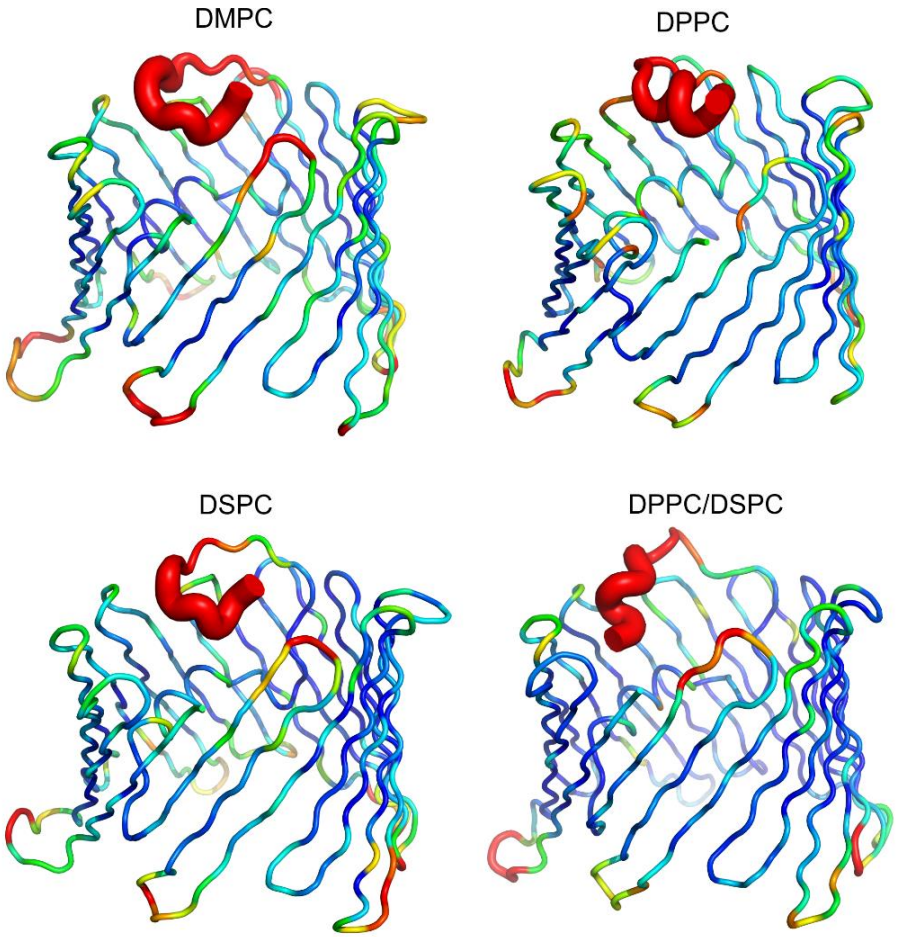

Figure S7. Sausage representation of hVDAC2 from the MDS in PC lipids. Shown here are the results from DMPC, DPPC, DSPC and DPPC/DSPC (DPDS) bilayer systems. DPPC shows the least fluctuation in the loop region. Further, the N-terminal extension is more structured in DPPC among all the lipid conditions. The extent of fluctuation seen is represented using the color gradient from blue (low fluctuation, LF) to red (high fluctuation, HF).

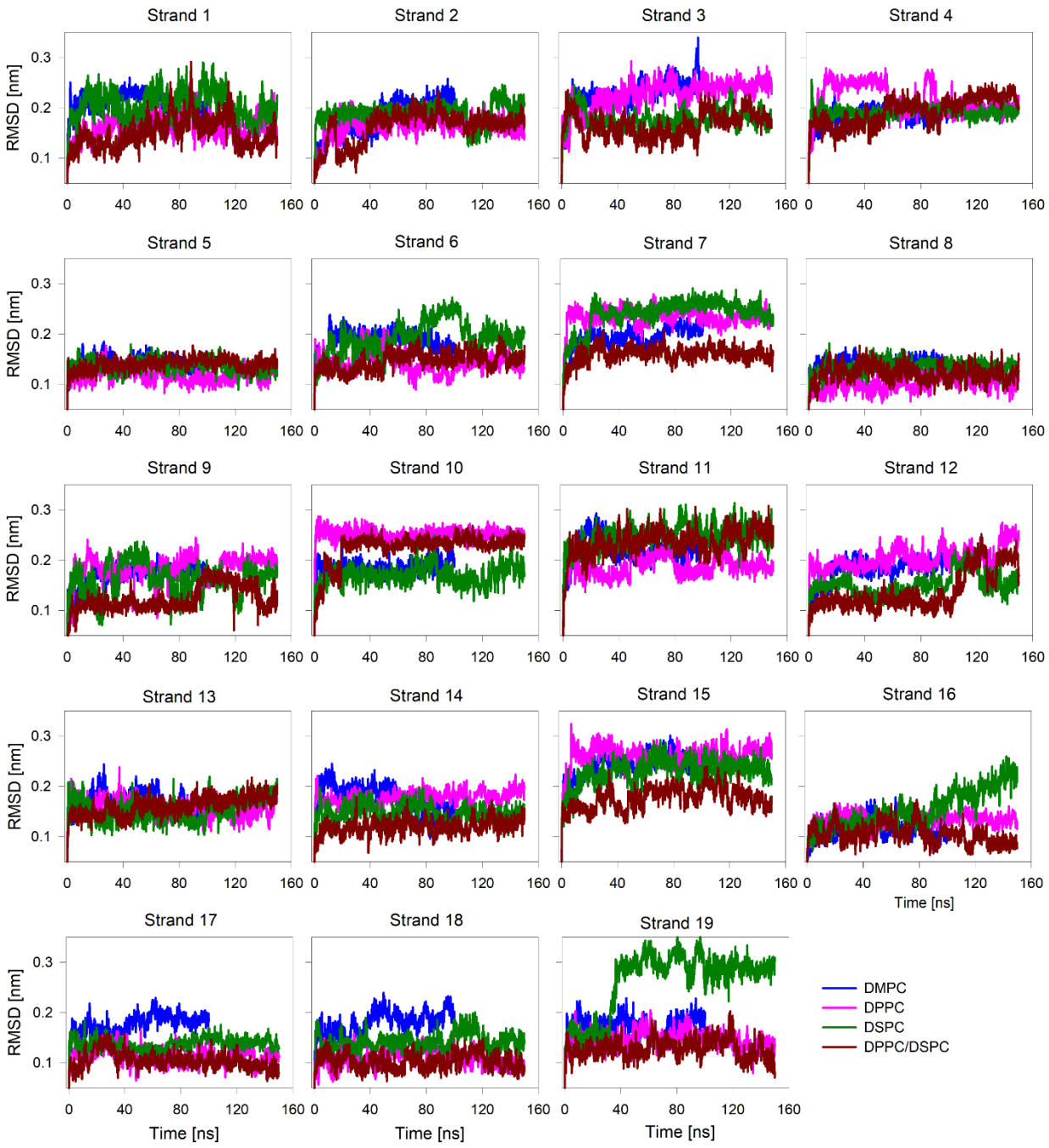

Figure S8. RMSD derived from all-atom MDS in lipids for hVDAC2. Shown here is the overlay of RMSD derived for every strand of hVDAC2 for all four lipidic bilayer system from 0-100/150 ns simulation trajectory. Color scheme used for each lipid is provided in the bottom right corner. The observed trend in the overall RMSD for the strands follows the order DPPC/DSPC < DPPC < DSPC < DMPC. While the RMSD for strands 10 and 15 are highest in DPPC, the overall RMSD of the entire protein (both strand and loop RMSD) is lowest in DPPC.

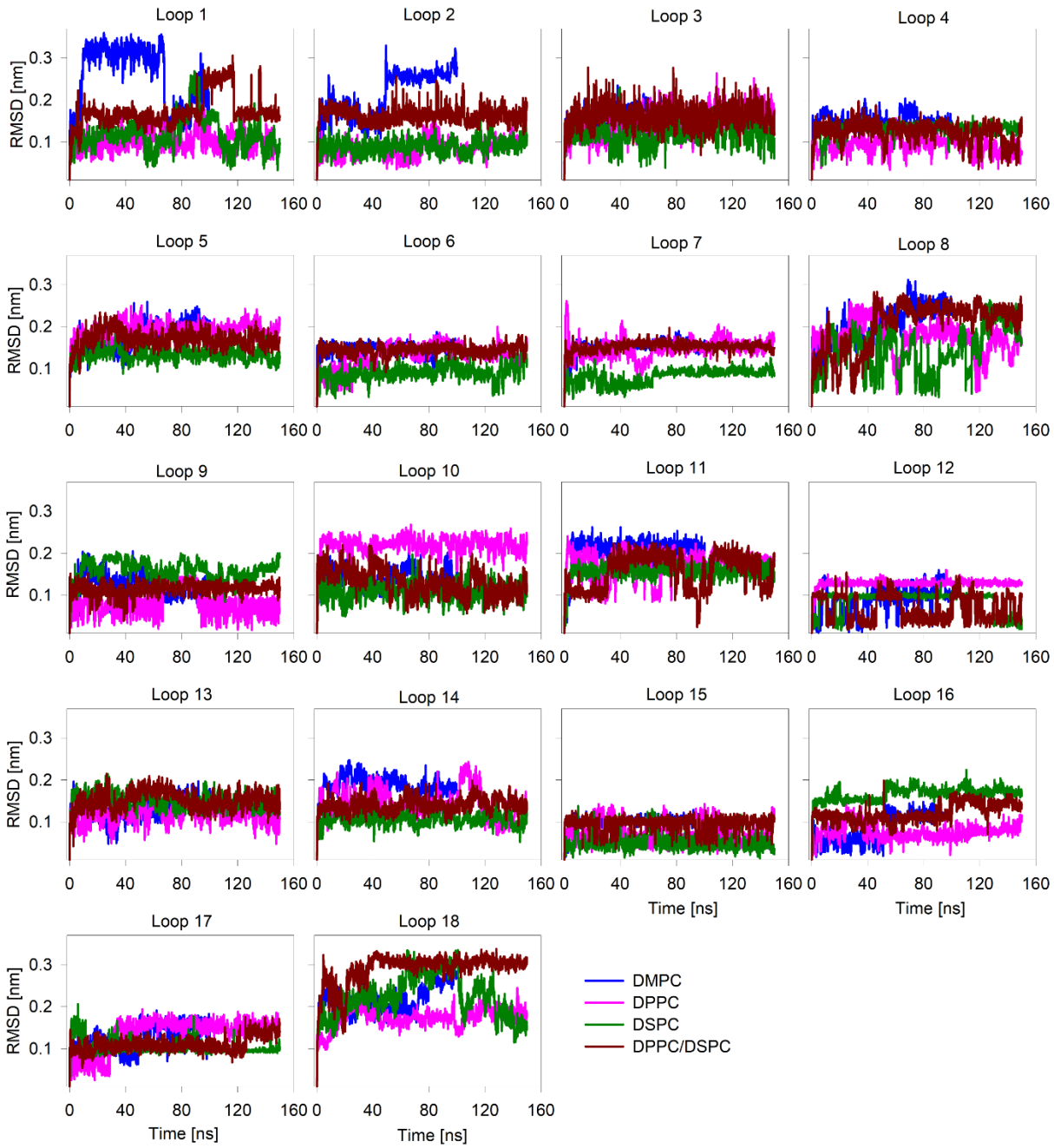

Figure S9. RMSD derived from all-atom molecular dynamics simulations in lipids for hVDAC2. Shown here is the overlay of RMSD derived for every loop region of hVDAC2 for all four lipid bilayer systems from 0-100/150 ns simulation trajectory. Color scheme used for each lipid is provided in the bottom right corner. The observed trend in RMSD follows the order DSPC < DPPC < DMPC < DPPC/DSPC, and the overall RMSD of the entire protein (both strand and loop RMSD) is lowest in DPPC. For example, when we compare DPPC and DMPC, the RMSD of only three loops, namely 9, 11 and 13, is higher in DPPC, while it is lower in the other fifteen loop regions. Similarly, compared with DSPC, only loops 7 and 13 exhibit higher fluctuation in DPPC, and the dynamics is lower in all other loops.

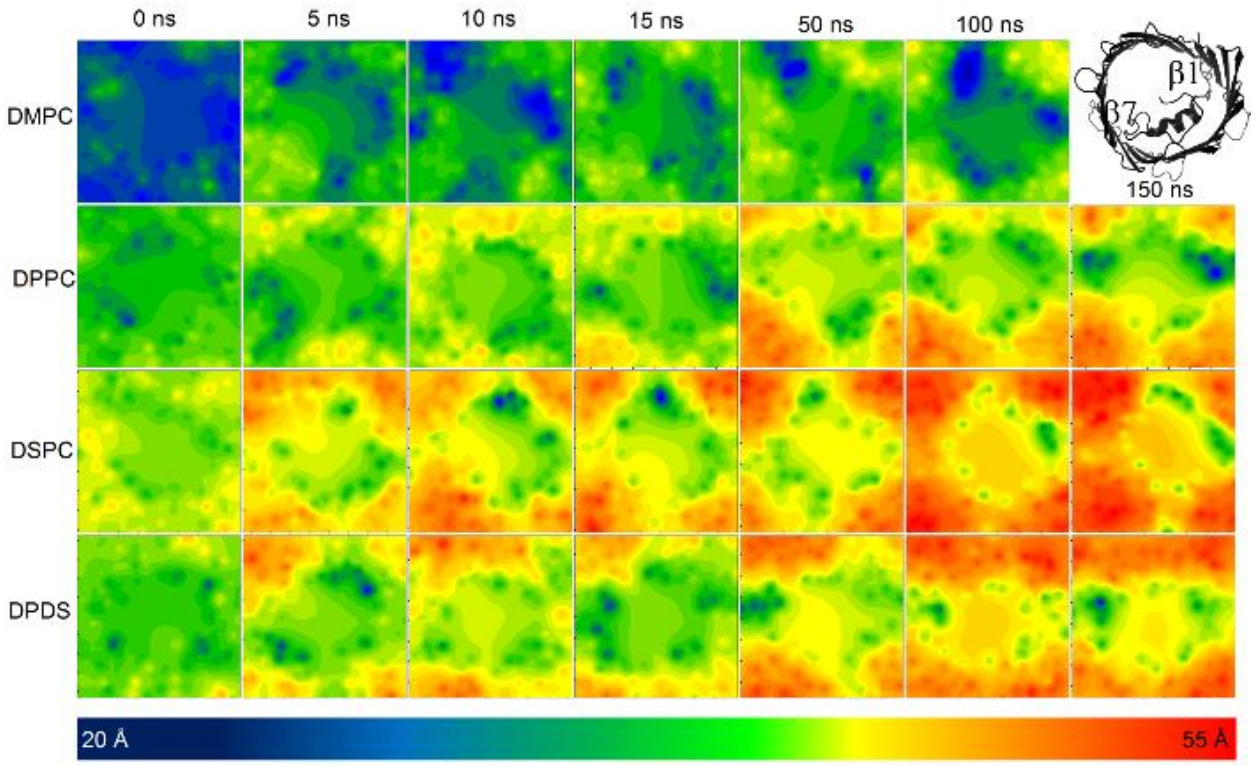

Figure S10. Lipid redistribution and change in membrane thickness with simulation time. Representative lipid thickness maps obtained from MEMBPLUGIN v1.1 (5) at 0, 5, 10, 15, 50, 100, and 150 ns of the simulation trajectory for all four lipid bilayers (DMPC, DPPC, DSPC, DPPC/DSPC (DPDS)). Each square is a two-dimensional representation of the simulation box. As the simulation progresses, we see a clear change in the bilayer thickness map, with thinning and thickening of specific membrane regions. The hVDAC2 barrel orientation was common in each bilayer thickness map, and is shown as a schematic (right top corner). The color scale and the corresponding lipid thickness range are provided below the composite image. Note that there is a known bug in the MEMBPLUGIN software, which calculates densities within the barrel, although no lipid is present (5). Hence, the lipid thickness map is only to be interpreted qualitatively.

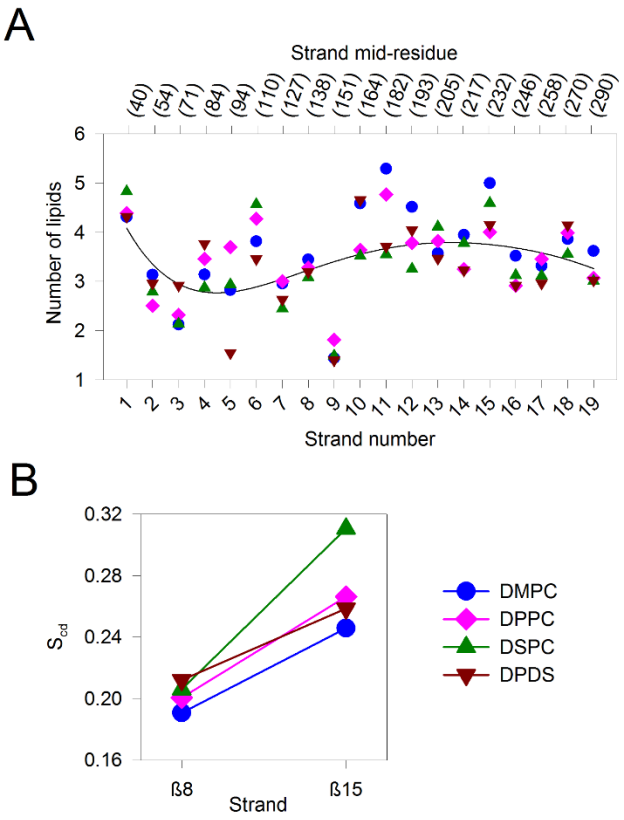

Figure S11. Asymmetric membrane thinning near specific barrel segments. (A) The number of lipid molecules (*y* axis) calculated in the 5 Å vicinity of the lipid-facing midplane residue of each strand (upper *x* axis) and for the complete strand (lower *x* axis) using the VMD TK-console script, is plotted here. The results show regions of the barrel where membrane thinning is evident (fewer lipid molecules) in all four lipid conditions (DMPC, DPPC, DSPC and DPPC/DSPC (DPDS)). The regression line is provided as a visual guide for the overall variation in lipid number across the hVDAC2 barrel. (B) Comparison of the lipid order parameter (S_{cd}) calculated for the mid residue of 8^{th} (membrane thinning region) and 15^{th} (membrane thickening region) strand. Lipid molecules in the 10 Å vicinity were used for the calculation. As expected, the S_{cd} is lowered near the 8^{th} strand, which supports membrane thinning in this region (note that membrane thinning creates lipid deformation and lowers the S_{cd}). S_{cd} is high near the 15^{th} strand where we see lipid thickening in all four lipid conditions.

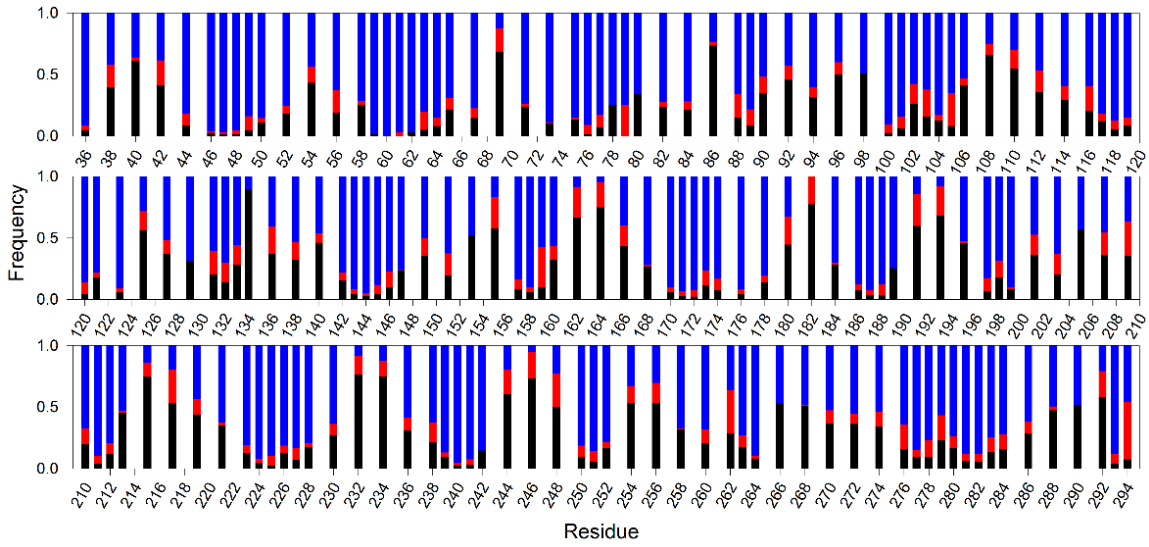

Figure S12. Vicinity analysis in hVDAC2-DMPC system. Frequency of occurrence each surrounding molecule (water, blue; lipid headgroup (P-atom), red; lipid hydrocarbon chain, black) near the 5 Å vicinity of all lipid facing strand residues, and all loop residues of hVDAC2 is plotted for DMPC bilayer system. Strand midplane residues are buried, and therefore show greater frequency of lipid acyl chain atoms. Similarly, interface and loop residues show greater occupancy of water and lipid head group in their vicinity.

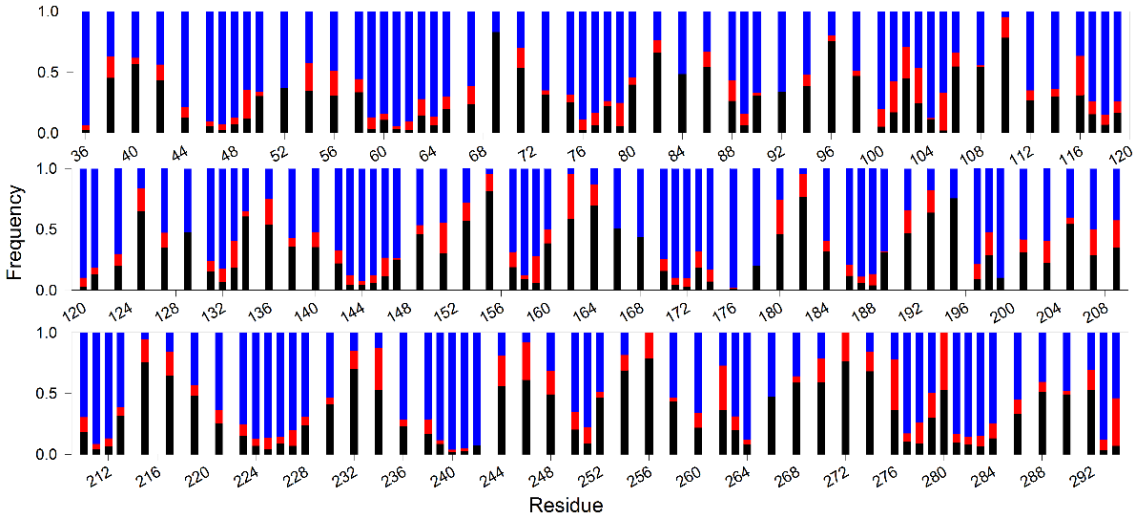

Figure S13. Vicinity analysis in hVDAC2-DPPC system. Frequency of occurrence each surrounding molecule (water, blue; lipid headgroup (P-atom), red; lipid hydrocarbon chain, black) near the 5 Å vicinity of all lipid facing strand residues, and all loop residues of hVDAC2 is plotted for DPPC bilayer system. Strand midplane residues are buried, and therefore show greater frequency of lipid acyl chain atoms. Similarly, interface and loop residues show greater occupancy of water and lipid head group in their vicinity.

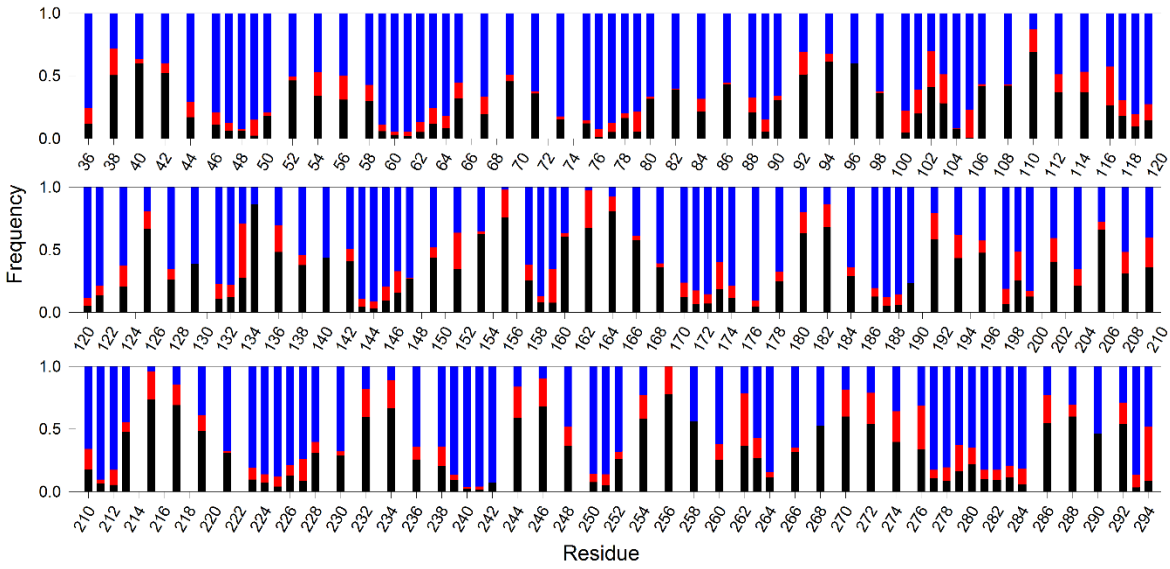

Figure S14. Vicinity analysis in hVDAC2-DSPC system. Frequency of occurrence each surrounding molecule (water, blue; lipid headgroup (P-atom), red; lipid hydrocarbon chain, black) near the 5 Å vicinity of all lipid facing strand residues, and all loop residues of hVDAC2 is plotted for DSPC bilayer system. Strand midplane residues are buried, and therefore show greater frequency of lipid acyl chain atoms. Similarly, interface and loop residues show greater occupancy of water and lipid head group in their vicinity.

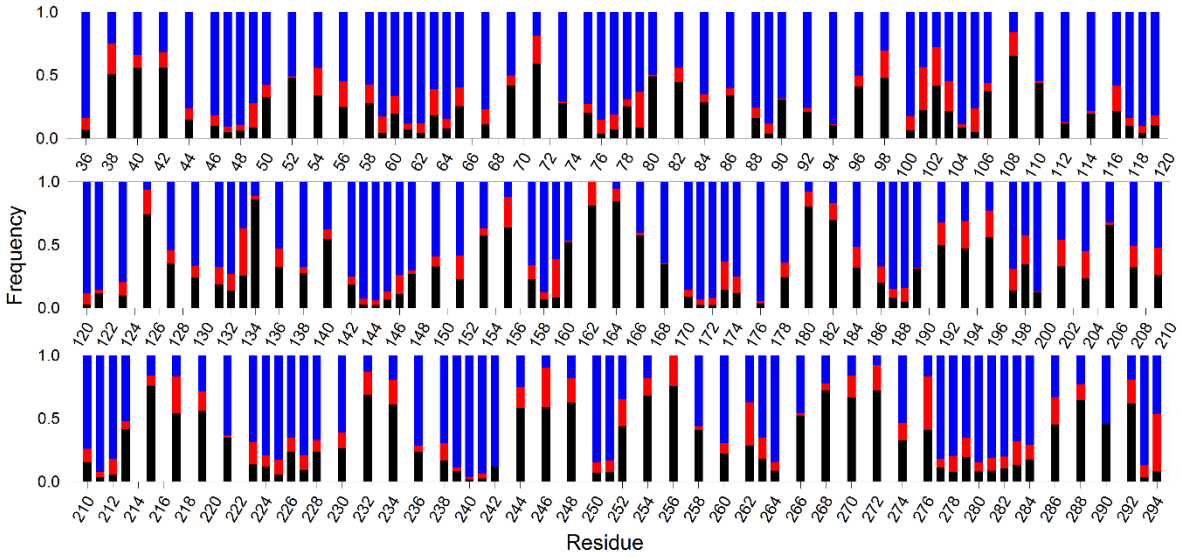

Figure S15. Vicinity analysis in hVDAC2-DPDS system. Frequency of occurrence each surrounding molecule (water, blue; lipid headgroup (P-atom), red; lipid hydrocarbon chain, black) near the 5 Å vicinity of all lipid facing strand residues, and all loop residues of hVDAC2 is plotted for the DPPC/DSPC bilayer system. Strand midplane residues are buried, and therefore show greater frequency of lipid acyl chain atoms. Similarly, interface and loop residues show greater occupancy of water and lipid head group in their vicinity.

Figure S16. Comparison of barrel deformation in various lipid bilayers. The hVDAC2 structures derived from 10 frames between the 50–100 ns simulation trajectory was averaged, and is shown here using the cartoon representation. Barrel structures in DMPC (top left, blue), DSPC (top right, green) and DPDS (bottom, brown) are overlaid here individually with the average structure in DPPC (pink). Overall, DPPC shows less deformation, while deformation of strands β3-β6 (shown as magnified image) is more pronounced in the other three lipids, particularly in DMPC.

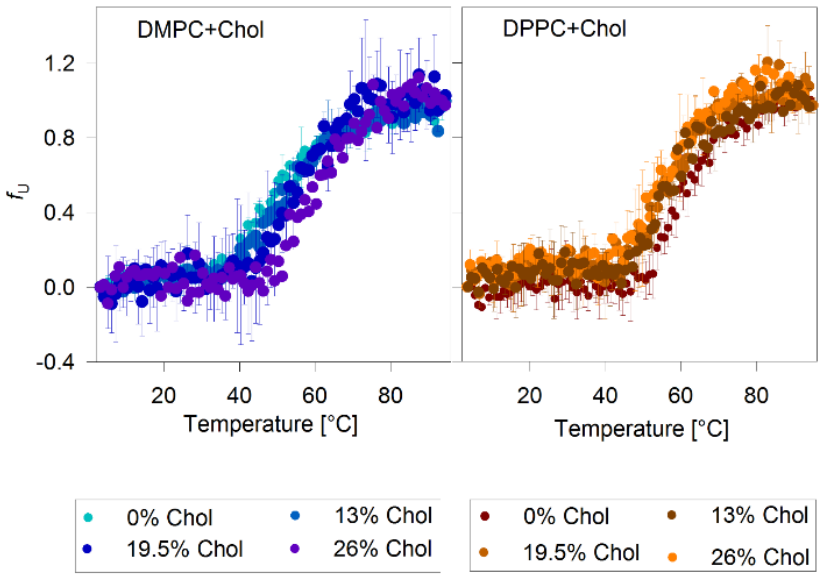

Figure S17. Effect of increasing cholesterol and acyl chain length on hVDAC2 stability. Dependence of the unfolded protein fraction (f_U) on temperature, derived from far-UV CD thermal unfolding at 215 nm is plotted here for q = 1.0 DMPC bicelles (left) and DPPC bicelles (right) with increasing cholesterol percentage. Color guides for both panels are shown below the plot. Error bars represent the s. d. calculated from 2-3 independent datasets. Data for DSPC:DPC bicelles is not shown here, as bicelles with higher percentages of cholesterol could not be prepared.

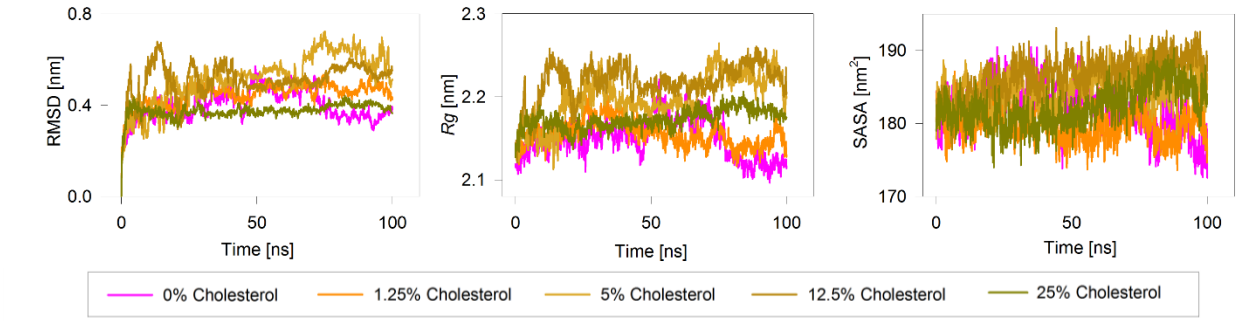

Figure S18. Parameters derived from all-atom molecular dynamics simulations in DPPC for hVDAC2 with increasing (0-25%) cholesterol content. Root mean square deviation (RMSD), radius of gyration (R_g) and solvent accessible surface area (SASA) derived for the full-length protein from the 100 ns simulations. The color/ symbol used for each condition is presented below the figure. RMSD for 0% cholesterol (pink line) and 25% cholesterol (green line) are comparable while it is higher in other cholesterol conditions. R_g and SASA do not show any significant change.

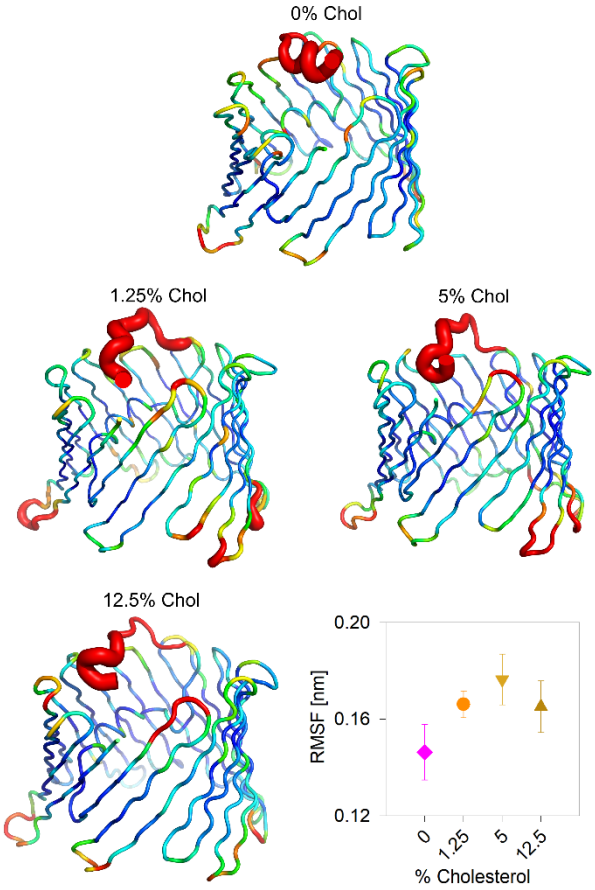

Figure S19. Sausage representation of hVDAC2 from the 100 ns MD simulations in DPPC bilayers with increasing cholesterol percentage. Shown here are the results from 0%–12.5% cholesterol (abbreviated as Chol). DPPC containing no cholesterol (0% Chol) shows the least fluctuation in the loop region. Further, the N-terminal extension is more structured in this condition. The extent of fluctuation seen is represented using the color gradient from blue (low fluctuation) to red (high fluctuation). Also shown is the plot of total RMSF with increasing cholesterol % (bottom right).

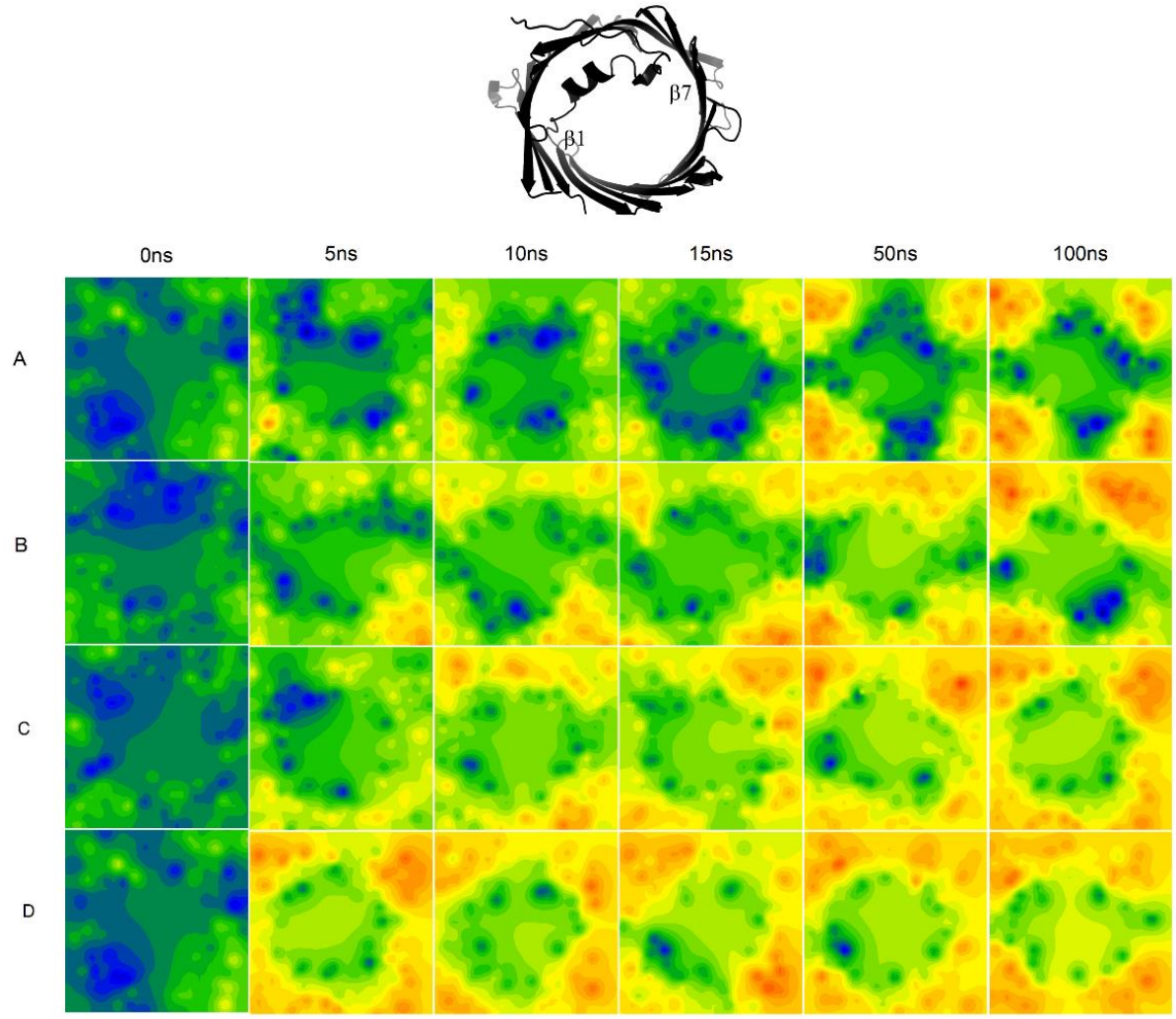

Figure S20. Lipid redistribution and change in membrane thickness with simulation time. Representative lipid thickness maps obtained from MEMBPLUGIN v1.1 (5) at 0, 5, 10, 15, 50, and 100 ns of the simulation trajectory for DPPC bilayers with increasing cholesterol content ((A) 1.25%, (B) 5%, (C) 12.5%, (D) 25% cholesterol). Each square is a two-dimensional representation of the simulation box. As the simulation progresses, the magnitude of change in the thickness map from the starting frame of the simulation to the last frame decreases with increasing cholesterol content. Hence, the membrane dynamicity is lowered when the cholesterol content of the DPPC bilayer increases. The hVDAC2 barrel orientation was common in each bilayer thickness map, and is shown as a schematic (top). The color scale and the corresponding lipid thickness range used in Figure S10 are retained here.

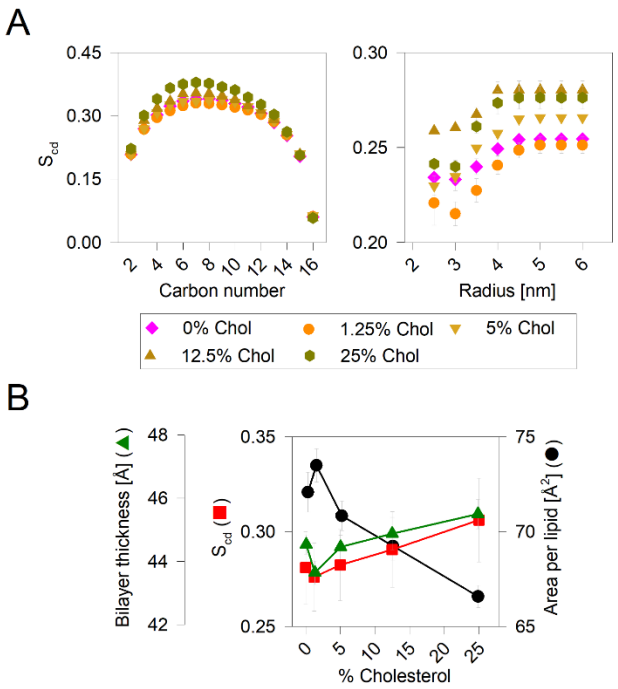

FIGURE S21. Effect of hVDAC2 on the DPPC bilayer physical property with increasing cholesterol content. (A) Bilayer S_{cd} was derived for 10 frames from 50–100 ns trajectory of the 100 ns MD simulation. Color/ symbol guide for the various cholesterol percentages is shown below plot (A). (Left) Average S_{cd} values for all 10 frames are plotted for each acyl carbon. As anticipated, the S_{cd} increases with increasing cholesterol content. (Right) Change in S_{cd} with distance from the hVDAC2 barrel center. S_{cd} is lowest near the protein, as protein creates deformation in the lipid membrane. (B) Average S_{cd}, APL and bilayer thickness derived from 10 frames of the 50–100 ns trajectory for the various cholesterol conditions. A prominent decrease in APL (black circle) is seen, while the S_{cd} (red squares) and bilayer thickness (green upward triangle) increases marginally.

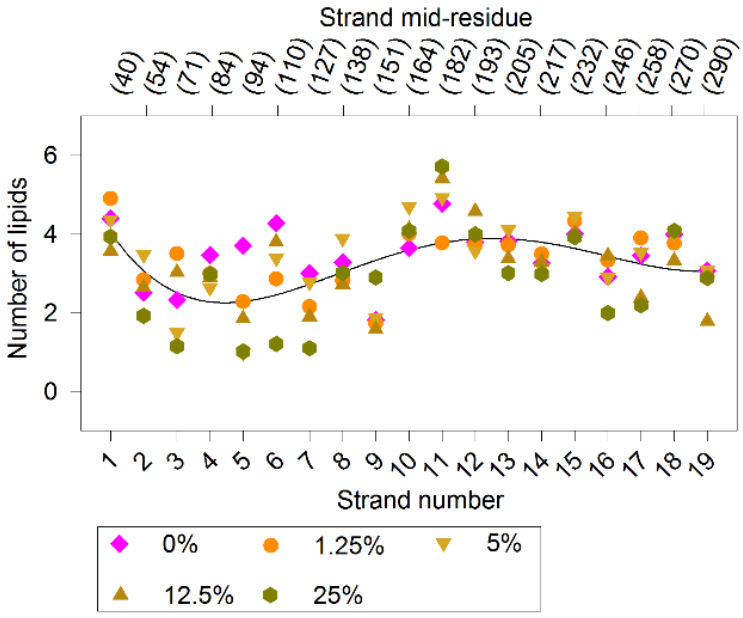

Figure S22. Asymmetric membrane thinning near specific barrel segments is retained in cholesterol with concomitant lowering in number of vicinal lipids. The number of lipid molecules (y-axis) calculated in the 5 Å vicinity of the lipid-facing midplane residue of each strand (upper x-axis) and for the complete strand (lower x-axis) using the VMD TK-console script, is plotted here. With increasing cholesterol content, the number of lipid molecules in the vicinity of strands β3-β7 is lowered compared to without cholesterol (0%). The regression line is provided as a visual guide for the overall variation in lipid number across the hVDAC2 barrel. Color/ symbol guide for the various cholesterol percentages is shown below the plot.

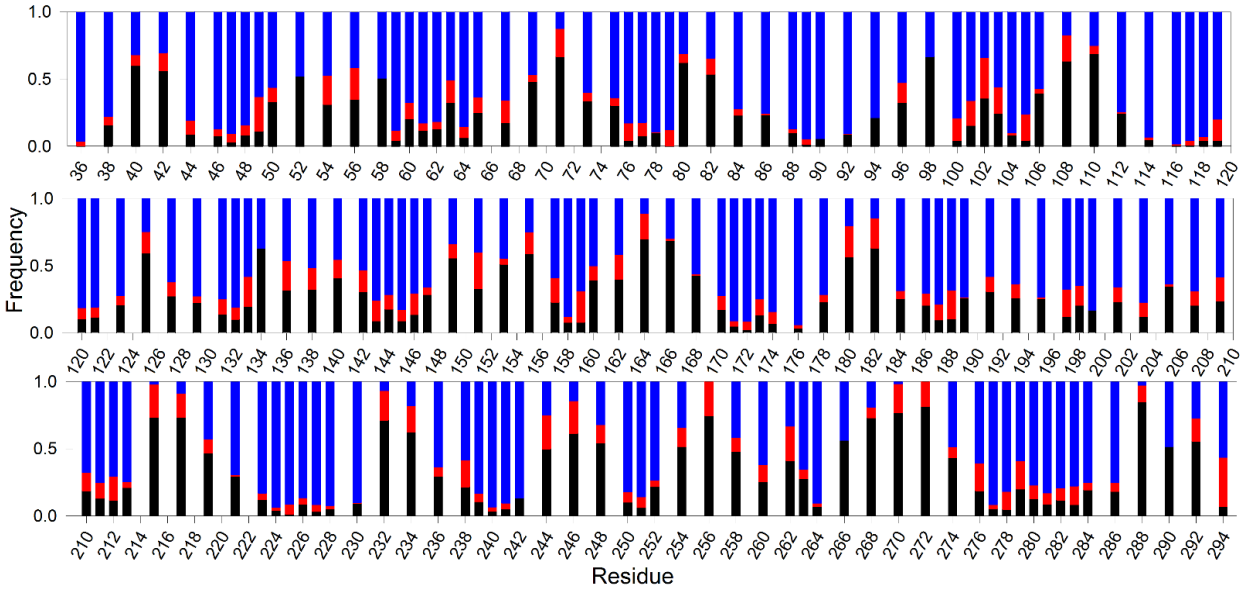

Figure S23. Vicinity analysis in hVDAC2-DPPC-1.25% cholesterol system. Frequency of occurrence each surrounding molecule (water, blue; lipid headgroup (P-atom), red; lipid hydrocarbon chain, black) near the 5 Å vicinity of all lipid facing strand residues, and all loop residues of hVDAC2 is plotted for DPPC-1.25% cholesterol bilayer system. Strand midplane residues are buried, and therefore show greater frequency of lipid acyl chain atoms. Similarly, interface and loop residues show greater occupancy of water and lipid head group in their vicinity.

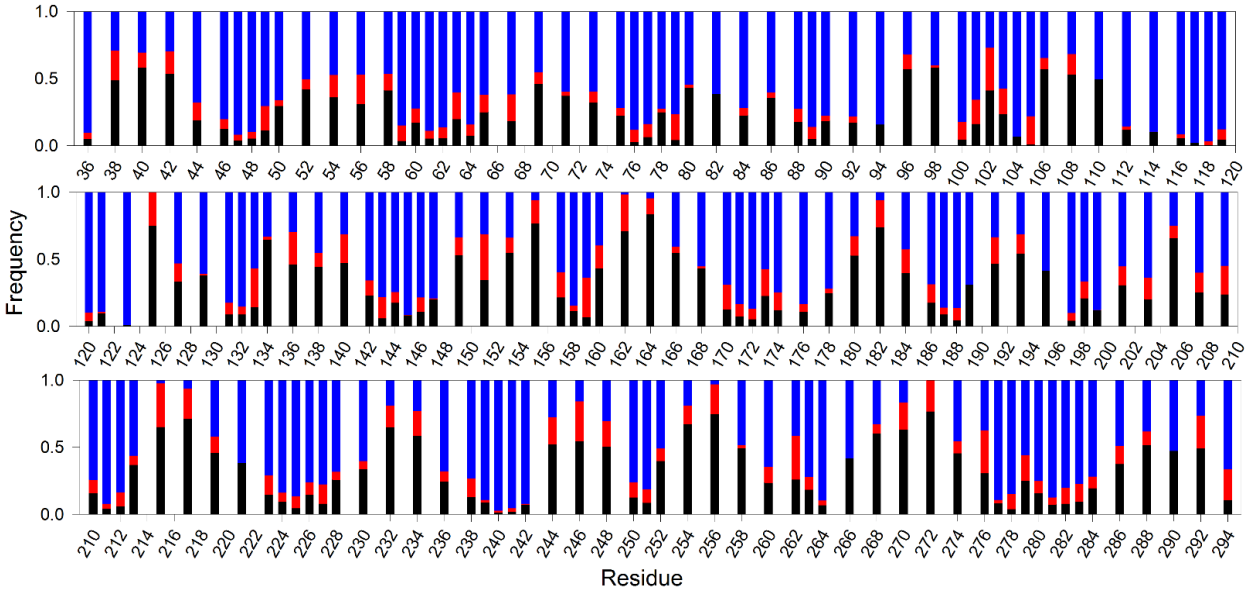

Figure S24. Vicinity analysis in hVDAC2-DPPC-5.0% cholesterol system. Frequency of occurrence each surrounding molecule (water, blue; lipid headgroup (P-atom), red; lipid hydrocarbon chain, black) near the 5 Å vicinity of all lipid facing strand residues, and all loop residues of hVDAC2 is plotted for DPPC-5% cholesterol bilayer system. Strand midplane residues are buried, and therefore show greater frequency of lipid acyl chain atoms. Similarly, interface and loop residues show greater occupancy of water and lipid head group in their vicinity.

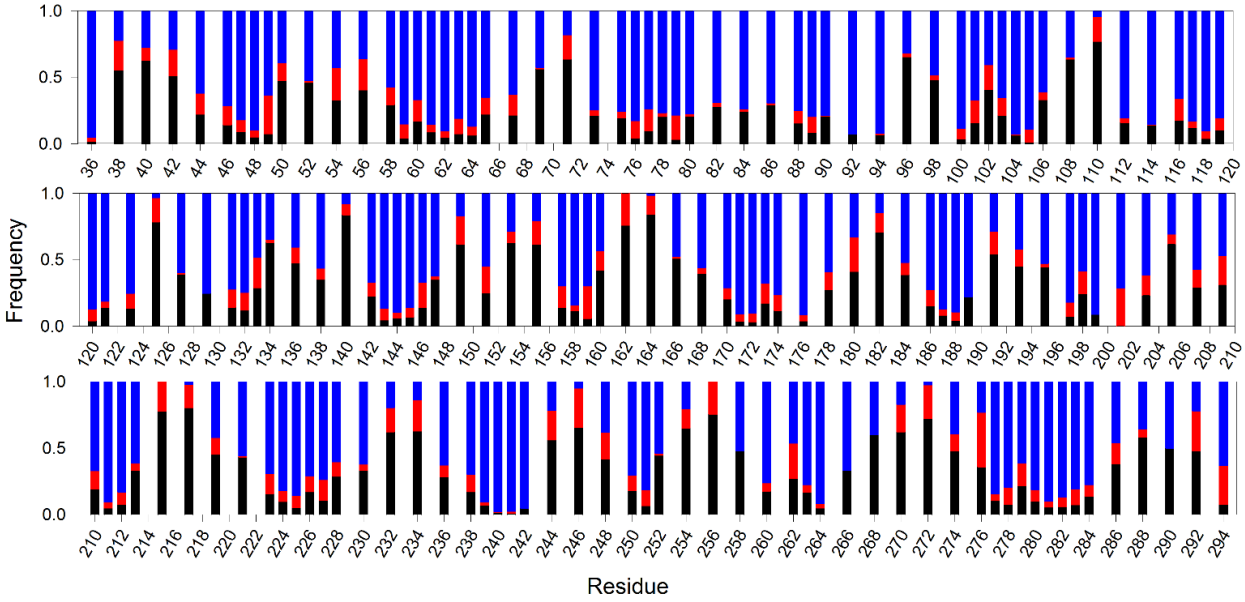

Figure S25. Vicinity analysis in hVDAC2-DPPC-12.5% cholesterol system. Frequency of occurrence each surrounding molecule (water, blue; lipid headgroup (P-atom), red; lipid hydrocarbon chain, black) near the 5 Å vicinity of all lipid facing strand residues, and all loop residues of hVDAC2 is plotted for DPPC-12.5% cholesterol bilayer system. Strand midplane residues are buried, and therefore show greater frequency of lipid acyl chain atoms. Similarly, interface and loop residues show greater occupancy of water and lipid head group in their vicinity.

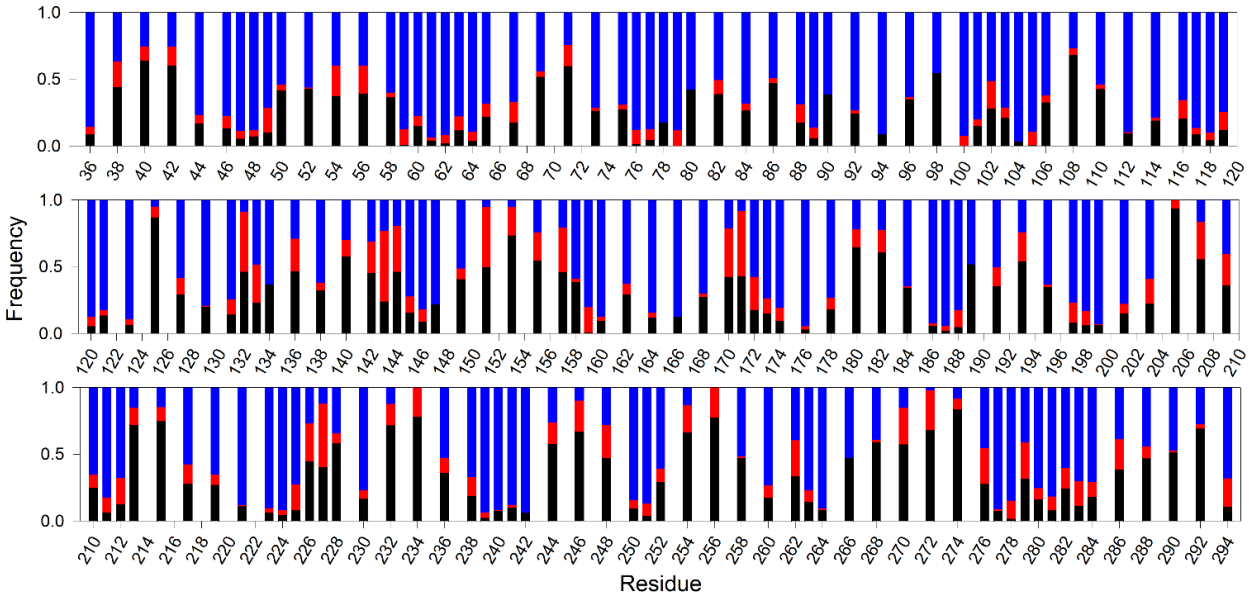

Figure S26. Vicinity analysis in hVDAC2-DPPC-25.0% cholesterol system. Frequency of occurrence each surrounding molecule (water, blue; lipid headgroup (P-atom), red; lipid hydrocarbon chain, black) near the 5 Å vicinity of all lipid facing strand residues, and all loop residues of hVDAC2 is plotted for DPPC-25% cholesterol bilayer system. Strand midplane residues are buried, and therefore show greater frequency of lipid acyl chain atoms. Similarly, interface and loop residues show greater occupancy of water and lipid head group in their vicinity.

SUPPORTING CITATIONS

1. Kucerka, N., M. P. Nieh, and J. Katsaras. 2011. Fluid phase lipid areas and bilayer thicknesses of commonly used phosphatidylcholines as a function of temperature. *Biochim. Biophys. Acta* 1808:2761-2771.
2. Maurya, S. R., and R. Mahalakshmi. 2013. Modulation of human mitochondrial voltage-dependent anion channel 2 (hVDAC-2) structural stability by cysteine-assisted barrel-lipid interactions. *J. Biol. Chem.* 288:25584-25592.
3. Maurya, S. R., and R. Mahalakshmi. 2015. N-helix and Cysteines Inter-regulate Human Mitochondrial VDAC-2 Function and Biochemistry. *J. Biol. Chem.* 290:30240-30252.
4. Silvius, J. R. 1982. Thermotropic Phase Transitions of Pure Lipids in Model Membranes and Their Modifications by Membrane Proteins. In Lipid-Protein Interactions. P. C. Jost, and O. H. Griffith, editors. John Wiley & Sons, Inc., New York. 239-281.
5. Guixa-Gonzalez, R., I. Rodriguez-Espigares, J. M. Ramirez-Anguita, P. Carrio-Gaspar, H. Martinez-Seara, T. Giorgino, and J. Selent. 2014. MEMBPLUGIN: studying membrane complexity in VMD. *Bioinformatics* 30:1478-1480.